1 Aerodynamic interaction of bristled wing pairs in fling

- Vishwa T. Kasoju¹ and Arvind Santhanakrishnan^{1, a)}
- School of Mechanical and Aerospace Engineering, Oklahoma State University,
- 4 Stillwater, OK 74078, USA
- 5 (Dated: 17 December 2020)

Tiny flying insects of body lengths under 2 mm use the 'clap-and-fling' mechanism with bristled wings for lift augmentation and drag reduction at chord-based Reynolds number (Re) on $\mathcal{O}(10)$. We examine wing-wing interaction of bristled wings in fling at Re=10, as a function of initial inter-wing spacing (δ) and degree of overlap between rotation and linear translation. A dynamically scaled robotic platform was used to drive physical models of bristled wing pairs with the following kinematics (all angles relative to vertical): 1) rotation about the trailing edge to angle θ_r ; 2) linear translation at a fixed angle (θ_t); and 3) combined rotation and linear translation. The results show that: 1) cycle-averaged drag coefficient decreased with increasing θ_r and θ_t ; and 2) decreasing δ increased the lift coefficient owing to increased asymmetry in circulation of leading and trailing edge vortices. A new dimensionless index, reverse flow capacity (RFC), was used to quantify the maximum possible ability of a bristled wing to leak fluid through the bristles. Drag coefficients were larger for smaller δ and θ_r despite larger RFC, likely due to blockage of inter-bristle flow by shear layers around the bristles. Smaller δ during early rotation resulted in formation of strong positive pressure distribution between the wings, resulting in increased drag force. The positive pressure region weakened with increasing θ_r , which in turn reduced drag force. Tiny insects have been previously reported to use large rotational angles in fling, and our findings suggest that a plausible reason is to reduce drag forces.

Keywords: bristled wing, fringed wing, clap and fling, fling, tiny insects, flapping flight

a) Electronic mail: askrish@okstate.edu

6 I. INTRODUCTION

The smallest insects (body length < 2 mm) such as thrips fly at a chord-based Reynolds number (Re) on the order of 10, representing what may be considered as the aerodynamic lower limit of flapping flight. Flight at such low Re is challenged by significant viscous dissipation of kinetic energy. To overcome viscous losses, tiny insects have to continuously flap their wings to stay aloft. These insects are observed to flap their wings at high frequencies ($\mathcal{O}(100 \text{ Hz})$), likely to increase Re by increasing their wing tip velocity. In contrast to larger insects such as hawkmoths and fruit flies, tiny insects are also observed to operate their wings at near-maximal stroke amplitudes and large pitch angles^{2,3}. At large stroke amplitudes, the wings of tiny insects come together in close proximity of each other at the end of upstroke ('clap') and move away from each other at the start of downstroke ('fling'). Since the discovery of 'clap-and-fling' by Weis-Fogh⁴ in the small chalcid wasp Encarsia Formosa, this mechanism has been observed in the free flight of other tiny insects such as the greenhouse whitefly⁵, thrips 6,7 , parasitoid wasps⁸ and jewel wasps⁸. A number of studies have explored the fluid dynamics of clap-and-fling experimentally⁹⁻¹¹, theoretically^{6,12,13}, and numerically^{7,13-17}, and have found that wing-wing interaction augments lift force through the generation of bound circulation at the leading edges of the wings during fling^{9,10,12,13,18}.

In contrast to larger flying insects where a stable leading edge vortex (LEV) is observed with a shed trailing edge vortex (TEV)¹⁹, previous studies of a single wing in linear translation¹⁴ and in semi-circular revolution²⁰ have shown that lift generation at $Re \sim 10$ is reduced due to 'vortical symmetry', where both the LEV and TEV remain attached to the wing. Miller and Peskin¹⁸ showed that lift enhancement by clap-and-fling is more pronounced for $Re \sim \mathcal{O}(10)$ than at higher Re, as most of the lift lost during the downstroke and upstroke (on account of vortical symmetry) can be recovered by establishing LEV-TEV vortical asymmetry during wing-wing interaction. However, at Re relevant to tiny insect flight, Miller and Peskin¹⁸ also showed that large drag penalties²¹ are associated with the fling. Subsequent studies have since shown that wing flexibility and the unique bristled structure of tiny insect wings can provide aerodynamic benefits by lowering drag forces needed to fling wings apart and increasing lift over drag ratio^{7,8,22–24}.

Forces generated by biological bristled structures such as tiny insect wings depend on inter-³⁴ bristle flow that is a function of Reynolds number based on bristle diameter (Re_b). Previous stud-³⁵ ies^{25,26} have shown that an array of bristles can undergo transition from acting as a leaky rake to ³⁶ a solid paddle with decreasing Re_b . Dynamically scaled models of bristled wings during transla-

tion and rotation have been reported to show little variation in forces in comparison with a solid wing 27,28 . Further, studies using comb-like wings 29,30 were found to generate almost the same amount of forces as a solid wing, with a 90% drop in wing weight. Recent studies using bristled wings $^{31-33}$ observed the formation of diffused shear layers around the bristles at smaller interbristle gaps. These shear layers prevent fluid from leaking through the inter-bristle gaps, resulting in the bristled wing behaving similar to a solid wing. A central limitation of the above studies is the lack of considering clap-and-fling kinematics observed in freely-flying tiny insects, involving aerodynamic interaction of bristled wing pairs. In our recent study 23 examining clap-and-fling for bristled wing pairs at $Re \sim \mathcal{O}(10)$, we found that leaky flow through the bristles results in design drag reduction and disproportionally lower lift reduction (i.e., improved lift over drag ratio) when compared to forces generated by geometrically equivalent solid wings. These aerodynamic benefits were diminished at Re=120 (relevant to larger fruit flies) 24 , suggesting that the use of clap-and-fling in conjunction with bristled wings is particularly well-suited at Re relevant to tiny insect flight.

In terms of wing-wing interaction of bristled wings, our recordings of free-takeoff flight of ₅₂ thrips show that these insects bring the wings close together (\sim 1/10-1/4 of chord length) at the ₅₃ end of upstroke (clap) before flinging the wings apart (**Figure 1**). Previous studies ^{16,17} have found 54 that increasing initial inter-wing spacing (δ in **Figure 1**, expressed non-dimensionally as % of 55 chord length) of interacting solid wings decreases aerodynamic forces. For δ >80%, interference ₅₆ effects between the wings were found to diminish. A high pressure region was observed to form 57 between the interacting solid wings during the end of the clap phase that generated a sharp peak 58 in forces at the end of clap and start of fling³⁴. However, none of these studies examined how ₅₉ inclusion of wing bristles impacts clap-and-fling aerodynamics under varying δ . The results of 60 these previous studies cannot be expected to be identical for bristled wing pairs performing similar δ_1 kinematics or for similar δ_2 , due to alterations in flow characteristics expected around and through 62 bristled wings. In addition, the above studies did not examine circulation of LEV and TEV and 63 corresponding effect on lift generation. In terms of wing motion, a recent study reported the 64 wing kinematics of free-flying thrips³ and noted large changes in pitch angle for small changes in 65 revolution of the wing. While this indicates that thrips wings may purely rotate at the start of fling 66 before translation, it remains unknown as to whether there are aerodynamic benefits associated 67 with such kinematics.

In this study, we aimed to examine how varying δ and wing kinematics impacts aerodynamic

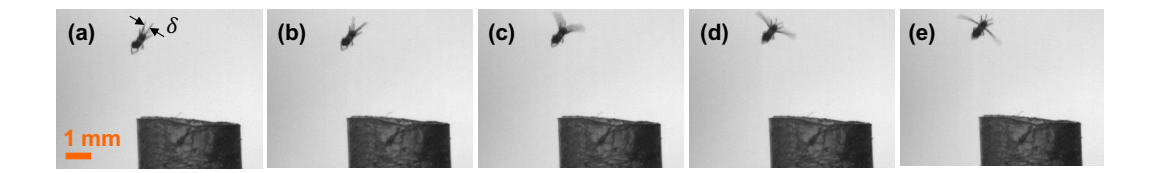


FIG. 1. Successive snapshots of thrips in free take-off flight. (a) End of upstroke ('clap') where the wings come in close proximity of each other, separated by non-dimensional inter-wing spacing δ . (b) Start of downstroke ('fling') where the wings move apart from each other, followed by the rest of the downstroke from (c) to (e). δ ranges from about 10% to 25% of the wing chord.

interaction of bristled wings during fling at Re=10. We used a dynamically scaled robotic platform fitted with a pair of physical bristled wing models for investigation. Aerodynamic force measurements and flow visualization were conducted for varying δ in the range of 10% to 50% of wing chord for three different kinematics: 1) wings purely rotating about their trailing edges; 2) linear translation of each wing at a fixed angle relative to the vertical; and 3) overlapping rotation and translation of each wing. In addition to clap-and-fling kinematics, tiny insects have been observed to employ 'rowing' kinematics in three-dimensional flapping flight, where the wings move fast downward and backward³⁵. As Re decreases (e.g., due to size reduction), the planar upstroke that is commonly employed by large scale insects changes to a U-shaped upstroke in tiny insects, with large changes in wing deviation from the stroke plane. This mechanism was found to generate 70% of the required vertical force for tiny insects. It is important to note that changes in deviation are not considered in this study.

81 II. METHODS

82 A. Dynamically scaled robotic platform

We comparatively examined the forces and flows generated during the prescribed motion of a pair of bristled wing physical models to those of a single bristled wing. The wing models were driven by a dynamically scaled robotic platform (**Figure 2(a)**) that has been used in our previous studies studies 23,24. For more details on the test platform, refer to **Appendix A**.

87 B. Bristled wing models

We fabricated a pair of rectangular scaled-up bristled wing models (**Figure 2(b)**) with wing span (S) of 81 mm and chord (c) of 45 mm. The bristled wing consisted of a 3 mm thick solid membrane (laser cut from optically clear acrylic) of length equal to S and 7 mm width (w), with 35 bristles of equal length (L_b =19 mm) attached on two opposite sides along the length of the membrane (70 bristles in total, in the range of tiny insects³⁶). The bristles consisted of approximately 0.20 mm diameter (D) 304 stainless steel wires, each being cut to length L_b . The inter-bristle gap (G) was maintained at 2 mm throughout the wing, to obtain G/D=10 in the range of G/D of tiny insect wings^{22,36}. An equivalent solid wing pair with the same S and C as the bristled wing was

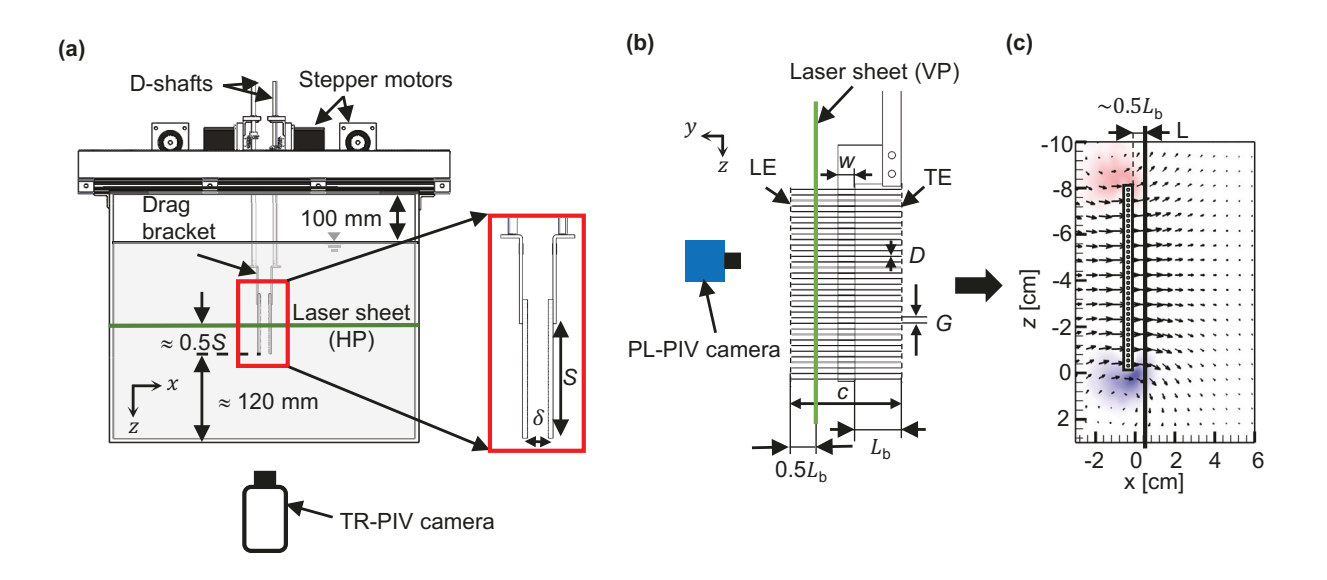


FIG. 2. Robotic platform and experimental setup used for force and PIV measurements. (a) Front view of the robotic platform with a pair of scaled-up physical bristled wing models separated by initial interwing spacing δ expressed non-dimensionally as % of wing chord (c). 2D TR-PIV setup with high-speed camera and laser sheet along a horizontal plane (HP). (b) Magnified view of rectangular bristled wing model showing 2D PL-PIV measurements using an sCMOS camera focused on a laser sheet along a vertical plane (VP). (c) Velocity vector fields obtained from 2D PL-PIV with vorticity contours overlaid on the top. L represents the line along which reverse flow capacity (RFC) was calculated. LE = leading edge; TE = trailing edge; x, y, z are fixed coordinate definitions; c=wing chord=45 mm; S=wing span=81 mm; total number of bristles=70; w=membrane width=7 mm; L_b =bristle length on each side of the membrane=19 mm.

96 also laser cut from optically clear acrylic for comparative measurements.

97 C. Kinematics

The robotic platform enabled rotation and linear translation of wing models along a horizontal stroke plane. We examined the isolated and combined roles of rotation and linear translation
in this study. Sinusoidal and trapezoidal motion profiles were used for wing rotation and translo1 lation, respectively (**Figure 3(a)**), using equations developed by Miller and Peskin¹⁸. The 2D
clap-and-fling kinematics developed by Miller and Peskin¹⁸ has been used in several previous
studies^{7,8,17,22,24}. The peak tip velocity (U_{max}) during rotation, linear translation and their combination was maintained constant throughout the study at 0.157 m s⁻¹. For tests examining wing
rotation, each wing model was rotated about its trailing edge (TE) from an initial vertical position
to an angle θ_r relative to the vertical (**Figure 3(b)**), reaching their peak angular velocity (ω_{max}) for
each θ_r . For the above U_{max} , the peak angular velocity (ω_{max}) was calculated using equation B1 in
Appendix B. The cycle duration (T) thus changed with varying θ_r (Table I). For tests examining
linear translation, each wing was preset prior to the start of wing motion to a fixed angle (θ_t) relaline tive to the vertical (**Figure 3(c)**) and the entire wing moved with the same velocity in a trapezoidal
motion profile reaching maximum tip velocity (U_{max}) of 0.157 m s⁻¹.

For tests examining combination of rotation and linear translation, each wing was prescribed to rotate and translate under varying levels of overlap (ζ) that was defined based on the start of wing translation relative to rotation (**Figure 3(a)**). Note that ζ =0% means that linear translation started at the end of rotation, and ζ =100% means that linear translation started at the same time as start of rotation. θ_{Γ} and θ_{τ} of 45° were used for all tests examining combined rotation and linear translation. ω_{max} for each ζ that was tested was equal to ω_{max} used in tests involving only wing rotation. T varied for each tested condition of combined rotation and linear translation (Table I). The wing motion for both the wings were identical but opposite in sign. Also, the motion was strictly two-dimensional (2D) without changes in the stroke plane. At the end of every cycle of each test condition, the wings were programmed to move back to the starting position and were paused for at least 30 seconds before starting the next cycle so as to remove the influence of cycle122 paused for at least 30 seconds before starting the next cycle so as to remove the influence of cycle123 to-cycle interactions. This pause time is applicable for all the data collection throughout the study.
124 A description of the mathematical equations used in modeling wing kinematics is provided in

126 D. Test conditions

Bristled wing pairs and a single bristled wing were tested at Re=10 for the following kinematics: 1) rotation to θ_r values of 22.5°, 45°, 67.5°; 2) linear translation at θ_t values of 0° (vertically oriented), 22.5°, 45°, 67.5°; and 3) combined rotation and linear translation for $\zeta=0\%$, 25%, 50%, 130 75%, 100%. Each of the above test conditions were repeated for $\delta=10\%$, 30%, 50% of wing chord (c) between the bristled wing pairs as well as in a single bristled wing (latter corresponding to $\delta\to\infty$). The wing models being tested were fully immersed in 99% glycerin solution. The kinematic viscosity (v) of the glycerin used in this study was measured using a Cannon-Fenske routine viscometer (size 400, Cannon Instrument Company, State College, PA, USA) to be 707 mm² s⁻¹ at room temperature. To obtain Re=10, peak velocity (U_{max}) was calculated to be 0.157

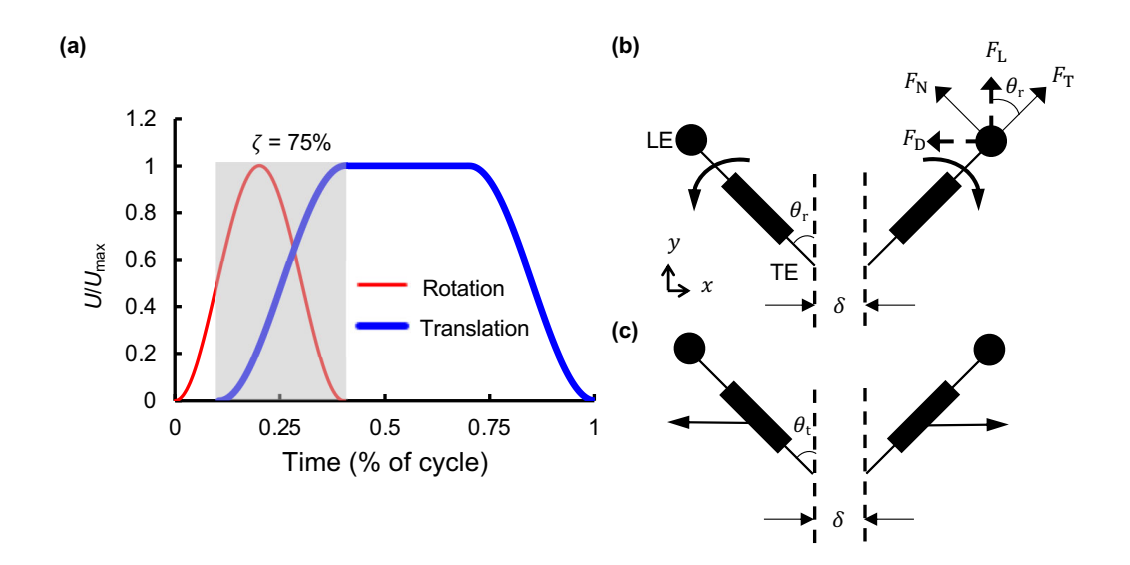


FIG. 3. Wing kinematics used in this study. (a) Time-varying motion profile for a single wing. Instantaneous wing tip velocity U was non-dimensionalized by peak tip velocity U_{max} . Time is expressed non-dimensionally in terms of percentage of cycle duration T. Thin and thick lines indicate rotational and translational motion, respectively. ζ indicates the percentage of overlap between wing rotation and the start of translation. (b) and (c) show sectional views of a bristled wing pair during wing rotation and linear translation, respectively. $\theta_{\rm r}$ is the angle at the end of wing rotation; $\theta_{\rm t}$ is the translation angle. Lift ($F_{\rm L}$) and drag ($F_{\rm D}$) forces were calculated

by taking components of tangential (F_T) and normal (F_N) forces in the vertical (F_L) and horizontal (F_D) directions.

 $_{136}$ m $_{8}^{-1}$ (and maintained constant as mentioned in subsection II C) using the following equation:

$$Re = \frac{U_{\text{max}}c}{v} \tag{1}$$

where c (**Figure 2(b)**) and v are constants. Using the kinematics equations provided in Miller and Peskin¹⁸, motion profiles were created to drive the stepper motors. Reynolds number based on bristle diameter D (defined as $Re_b = U_{\text{max}}D/v$) was also maintained constant at 0.045 throughout the study, which is in the range of thrips $(0.01-0.07)^{22}$.

141 E. Force measurements

Similar to our previous studies^{23,24}, force data were collected using uniaxial strain gauges mounted on both sides of custom L-brackets in half-bridge configuration. The L-brackets were used to couple a wing to the D-shaft (see **Appendix A** for details of test platform). A strain gauge conditioner continuously measured the forces in the form of voltage signals based on L-bracket deflection during wing motion. For more details of force measurements, refer to **Appendix C**.

147 F. Flow visualization

We conducted 2D time-resolved particle image velocimetry (2D TR-PIV) measurements to visualize time-varying chordwise flow generated by the motion of a wing pair (or a single wing) at a horizontal plane (HP) located at mid-span (**Figure 2(a)**). 2D TR-PIV based 2-component velocity vector fields were also used to determine the strength of the LEV and TEV, net circulation on a wing and pressure distribution in the flow field. In addition, 2D phase-locked PIV (2D PL-PIV) measurements were conducted to characterize the inter-bristle flow along the wing span at a vertical plane (VP) located at $0.5L_b$ measured from the leading edge (LE) as shown in **Figure 2(b)**. For more details on 2D TR-PIV, 2D PL-PIV and PIV processing, refer to **Appendices D**, **E**, **F**, for respectively.

157

Kinematics	Cycle duration	Frame rate
	T [ms]	[Hz]
Rotation, $\theta_{\rm r}$ [°]		
22.5	250	400
45	500	200
67.5	750	133.33
Translation, θ_t [°]		
0	1110	90
22.5	1110	90
45	1110	90
67.5	1110	90
Overlap, ζ [%]		
0	1610	61.72
25	1490	67.11
50	1360	73.52
75	1240	80.64
100	1110	90.09

TABLE I. Experimental test conditions, cycle duration and TR-PIV frame rates used for: rotation (θ_r), translation (θ_t), and overlapping rotation and translation (ζ in %). Note that ζ =0% indicates translation starts at the end of rotation, and ζ =100% indicates translation starts at the same time as start of rotation.

158 G. Definitions of calculated quantities

159 1. Lift and drag coefficients

Lift force (F_L) and drag force (F_D) were defined along the vertical and horizontal directions, 161 respectively, and calculated using non-simultaneous measurements of tangential (F_T) and normal 162 (F_N) forces (**Figure 3(b)**). F_T and F_N measurements were phase-averaged over 30 cycles for 163 further analyses of F_L and F_D . We acquired 30 cycles of force data to account for variability in 164 the mechanical operation of our robotic platform, and characterized this variability using standard 165 deviation across the 30 cycles. Dimensionless lift coefficient (C_L) and drag coefficient (C_D) were 166 calculated using components of measured F_N and F_T using the following equations:

$$C_{\rm L} = \frac{F_{\rm L}}{0.5\rho U_{\rm max}^2 A} = \frac{F_{\rm T} \cos\theta + F_{\rm N} \sin\theta}{0.5\rho U_{\rm max}^2 A}$$
(2)

167

$$C_{\rm D} = \frac{F_{\rm D}}{0.5\rho U_{\rm max}^2 A} = \frac{F_{\rm T} \sin\theta + F_{\rm N} \cos\theta}{0.5\rho U_{\rm max}^2 A}$$
(3)

where θ is the instantaneous angular position of the wing relative to the vertical and ρ is the density of the fluid medium (ρ of the glycerin solution used in this study was measured to be 1259 kg m⁻³).

171 2. Circulation

Circulation was calculated to quantify the strength of the LEV and TEV using the z-component of vorticity (ω_z). ω_z was calculated from the exported phase-averaged TR-PIV velocity fields using the following equation implemented in a custom MATLAB script:

$$\omega_z = \frac{\partial v}{\partial x} - \frac{\partial u}{\partial y}.\tag{4}$$

Circulation (Γ) was calculated from ω_z fields at all time instants and test conditions where TR-PIV data were acquired, using the following equation in a custom MATLAB script:

$$\Gamma = \iint_{S} \omega_{z} \, ds \tag{5}$$

the maximum absolute values of ω_z (i.e., $|\omega_z|$) at both LEV and TEV of a bristled wing were identified. A 15% $|\omega_z|$ high-pass cut-off was next applied to isolate the vortex cores on a single bristled wing performing the same kinematics. Alternative cutoff values of 5% and 25% of $|\omega_z|$ were examined for one condition each of rotation (θ_r =22.5°), linear translation (θ_t =22.5°) and combined rotation and translation (ζ =25%) and the resulting time-variation of Γ are provided as supplementary material (**Figure S1**). The trend of time-variation of Γ was unaffected when changing cutoff from 15% $|\omega_z|$ (**Figure 20**) to 25% $|\omega_z|$ (**Figure S1** (b),(d),(f)), with only small changes in the magnitude. However, for a lower cutoff of 5% $|\omega_z|$, we observed slight variation in the time-variation of Γ at the expense of undesirable high-frequency noise. We thus used 15% $|\omega_z|$ as the cutoff for circulation analyses presented in this study. Γ of LEV or TEV was then calculated by selecting a region of interest (ROI) by drawing a box around a vortex core. A custom MATLAB

mm side. If the circulation values matched between the 2 boxes, then we stopped further iteration. If the circulation values did not match between the 2 boxes, we increased the size of the smaller box by 3 mm and iterated the process. When calculating Γ of a specific vortex (LEV or TEV), we ensured that ω_z of the oppositely-signed vortex was zeroed out. For example, ω_z of the negatively-signed TEV was zeroed out when calculating the Γ of the positively-signed LEV on the right wing of a wing pair in fling. This allowed us to work with one particular vortex at a time and avoids contamination of the Γ estimation, if the box were to overlap with the region of the oppositely-signed vortex. Γ in this study is presented for left wing only, assuming the following: (a) Γ_{LEV} on the right wing is equivalent to Γ_{LEV} of left wing but oppositely signed; (b) Γ_{TEV} on the right wing is equivalent to Γ_{LEV} of left wing but oppositely signed. It is important to note that asymmetry in Γ_{LEV} and Γ_{TEV} for the *same* wing is to be expected as in previous studies of wing-wing interaction at low Re on the order of $10^{17,18,24}$. Γ at the LEV and TEV for all the test conditions were negative and positive, respectively, for the left wing.

In addition to Γ_{LEV} and Γ_{TEV} , we also calculated cycle-averaged net circulation ($\overline{\Gamma}_{net}$) on the left wing using the following equation.

$$\overline{\Gamma_{\text{net}}} = \overline{|\Gamma_{\text{LEV}}| - |\Gamma_{\text{TEV}}|} \tag{6}$$

As 2D, 2-component TR-PIV measurements were used to calculate Γ_{LEV} , Γ_{TEV} and $\overline{\Gamma}_{net}$, we examined the validity of 2D flow simplification by computing 2D divergence of the TR-PIV based velocity fields along the *x-y* plane. We observed small regions of non-zero 2D divergence in the flow field, suggesting that 2D flow simplification was reasonable for this study. For more details, refer to Appendix G.

211 3. Downwash velocity

Downwash velocity ($\overline{V_y}$) was defined as the spatially-averaged velocity of the flow deflected downward by the motion of a bristled wing pair. $\overline{V_y}$ calculated using the following equation from spatiall-averaged TR-PIV velocity vector fields:

$$\overline{V_y} = \frac{1}{N} \left[\sum_{\text{FOV}} v(x, y) \right] \tag{7}$$

where v(x, y) is the vertical component of velocity and N is the total number of grid points within the TR-PIV field of view (FOV).

217 4. Pressure distribution and average pressure coefficient

Using the algorithm developed by Dabiri et al.³⁸, unsteady pressure (*p*) distribution was es²¹⁹ timated from TR-PIV velocity vector fields. The pressure distribution presented in this study is
²²⁰ calculated using direct integration of the pressure gradient term in the Navier–Stokes equation (for
²²¹ more details, see Dabiri et al.³⁸). The pressure estimation in this study includes the viscous terms
²²² in the Navier–Stokes equation. This estimated pressure distribution was visualized in Tecplot soft²²³ ware. In addition, we also calculated the spatially-averaged positive and negative pressures across
²²⁴ the entire phase-averaged TR-PIV FOV at every time instant using the following equations:

$$\overline{p_{+}} = \frac{1}{N_{+}} \left[\sum_{\text{FOV}} p_{+}(x, y) \right] \tag{8}$$

225

$$\overline{p_{-}} = \frac{1}{N_{-}} \left[\sum_{\text{FOV}} p_{-}(x, y) \right] \tag{9}$$

where $\overline{p_+}$ and $\overline{p_-}$ are the spatially-averaged positive pressure and spatially-averaged negative pressure, respectively, estimated in the entire TR-PIV FOV at a particular timepoint. N_+ and N_- are the total number of grid points in (x,y) of the portion of the FOV containing positive and negative pressures, respectively.

Using the spatially-averaged positive and negative pressures, an spatially-averaged coefficient of pressure $(\overline{C_p})$ was calculated using the following equation:

$$\overline{C_p} = \frac{2 \, \overline{p}}{\rho U_{\text{max}}^2} \tag{10}$$

where \overline{p} is the spatially-averaged positive or negative pressure calculated from equations (8) and (9).

In addition to the above spatially averaged pressure coefficient $(\overline{C_p})$, we also calculated the cycle-averaged net pressure coefficient $(\overline{C_{p,net}})$ using the following equation:

$$\overline{C_{p,\text{net}}} = \frac{2 |\overline{||p_{+}| - |p_{-}||}}{\rho U_{\text{max}}^{2}}$$
(11)

where $\overline{p_+}$ is the spatially averaged positive pressure calculated from equation (8), $\overline{p_-}$ is the spatially averaged negative pressure calculated from equation (9), ρ is the density of the fluid medium

²³⁸ and U_{max} is the maximum tip velocity during translation or rotation (maintained constant throughout the study at 0.157 m s⁻¹.

240 5. Reverse flow capacity (RFC)

Inter-bristle flow along the wing span is influenced by Re_b , G, D and wing inclination relative to the flow. Significant changes can be expected in the Re_b range of tiny insect flight, such that the wing bristles can permit fluid leakage or behave like a solid plate. From the PL-PIV velocity fields, we estimated the capacity of a bristled wing to leak flow (in the direction opposite to wing motion) by comparing the volumetric flow rate (per unit width) along the wing span to that of a geometrical cally equivalent solid wing undergoing the same wing motion. Reverse flow capacity (RFC) was calculated along a line 'L' parallel to the span and located at a distance of $\sim 50\% L_b$ (Figure 2(b)). Volumetric flow rate per unit width for a particular wing model (Q_{wing}) was calculated using the following equation:

$$Q_{\text{wing}} = \int_{L} u \, dz \tag{12}$$

where u denotes the horizontal component of velocity along line 'L'. RFC was calculated using the following equation:

$$RFC [\%] = \frac{Q_{\text{solid}} - Q_{\text{bristled}}}{Q_{\text{solid}}}$$
(13)

where Q_{solid} and Q_{bristled} represents the volumetric flow rate per unit width displaced by a solid wing and bristled wing undergoing the same motion, respectively. The reason underlying calculation of reverse flow capacity (RFC) was to understand the ability of a bristled wing to leak the fluid through the gaps by comparing it to a solid wing of identical chord and span when both wing models are undergoing the same wing motion. We expect that reverse flow would be larger closer to the leading edge (LE) of the wing during rotation, when the wing is being rotated with respect to trailing edge (TE). During translation, as the entire wing is translating at the same velocity, the reverse flow through the entire wing at any y-location in x-z plane can be assumed to be the same. Considering the above factors, we chose a laser plane closer to LE of the wing. From our previous study²³, we observed no flow along the z-direction of a rectangular bristled wing model (Figure 2(b)). We thus expected that using only the x-velocity component would be sufficient to characterize RFC. To verify the lack of z-directional flow in this study, we looked at the velocity vector field (overlaid with vorticity contours) for one condition of rotation, translation and overlap

for a single wing and a wing pair with inter-wing spacing (δ) = 10% (see Supplementary Material, Movies 1, 2, 3). We observed no flow along the *z*-direction.

267 III. RESULTS

268 A. Bristled wings in rotation

Aerodynamic force generation. In general, both C_L and C_D followed the kinematic profile of rotational motion (**Figure 4(a)-(d)**). When θ_r was increased from 22.5° to 67.5°, C_D and C_L peaks occurred earlier in time (**Figure 4(c),(d)**). With increasing θ_r , relatively we observed analogous reduction in C_D and C_L . A noticeable drop in C_D was observed with increasing δ for all θ_r . C_L was highest for the lowest initial inter-wing spacing (δ =10%) in both θ_r =22.5° (**Figure 4(b)**) and θ_r =67.5° (**Figure 4(d)**). Increasing δ from 10% to 30% resulted in a noticeable drop in C_L , following which C_L showed minimal variation for δ =50% as well as the single wing (**Figure 4(b),(d)**). This insensitivity of C_L for $\delta \geq 30\%$ was in sharp contrast to C_D variation with δ (**Figure 4(a),(c)**). To dropped below zero toward the end of the cycle for θ_r =22.5° (**Figure 4(a)**), likely due to wing deceleration altering flow around the bristled wing model in a short time span. With increase in θ_r to 67.5°, the magnitude of negative drag was decreased (**Figure 4(c)**).

Cycle-averaged drag coefficient $(\overline{C_D})$ decreased with increasing θ_r (**Figure 4(e)**). Increasing θ_r from 22.5° to 67.5° for the single wing showed little to no variation in $\overline{C_D}$. By contrast, the bristled wing pair with lowest δ (=10%) showed substantial decrease in $\overline{C_D}$ with increasing θ_r . With further increase in δ , $\overline{C_D}$ decreased with θ_r and approached single wing values. Similar to $\overline{C_D}$, also decreased with increasing θ_r . Increasing δ beyond 10% resulted in little to no variation in $\overline{C_L}$. Finally, with increasing δ , larger reduction in C_D was observed compared to smaller reduction in C_L for $\delta > 10\%$.

287 <u>Chordwise flow.</u> Rotation of a single bristled wing generated a pair of counter-rotating vortices at the LE and TE (**Figure 5**). For the three θ_r values that we examined, we observed both the LEV and TEV to be attached to the wing. Increasing θ_r promoted earlier development of the LEV and TEV (compare **Figure 5(a),(e),(i)**). At 50% (**Figure 5(b),(f),(j)**) and 75% of the cycle (**Figure 5(c),(g),(k)**), increasing θ_r was found to diffuse the vorticity in both the LEV and TEV cores and dissipating at the end of the cycle (**Figure 5(d),(h),(l)**).

For a bristled wing pair that was rotated to θ_r =22.5°, increasing δ from 10% (**Figure 6(a)**-

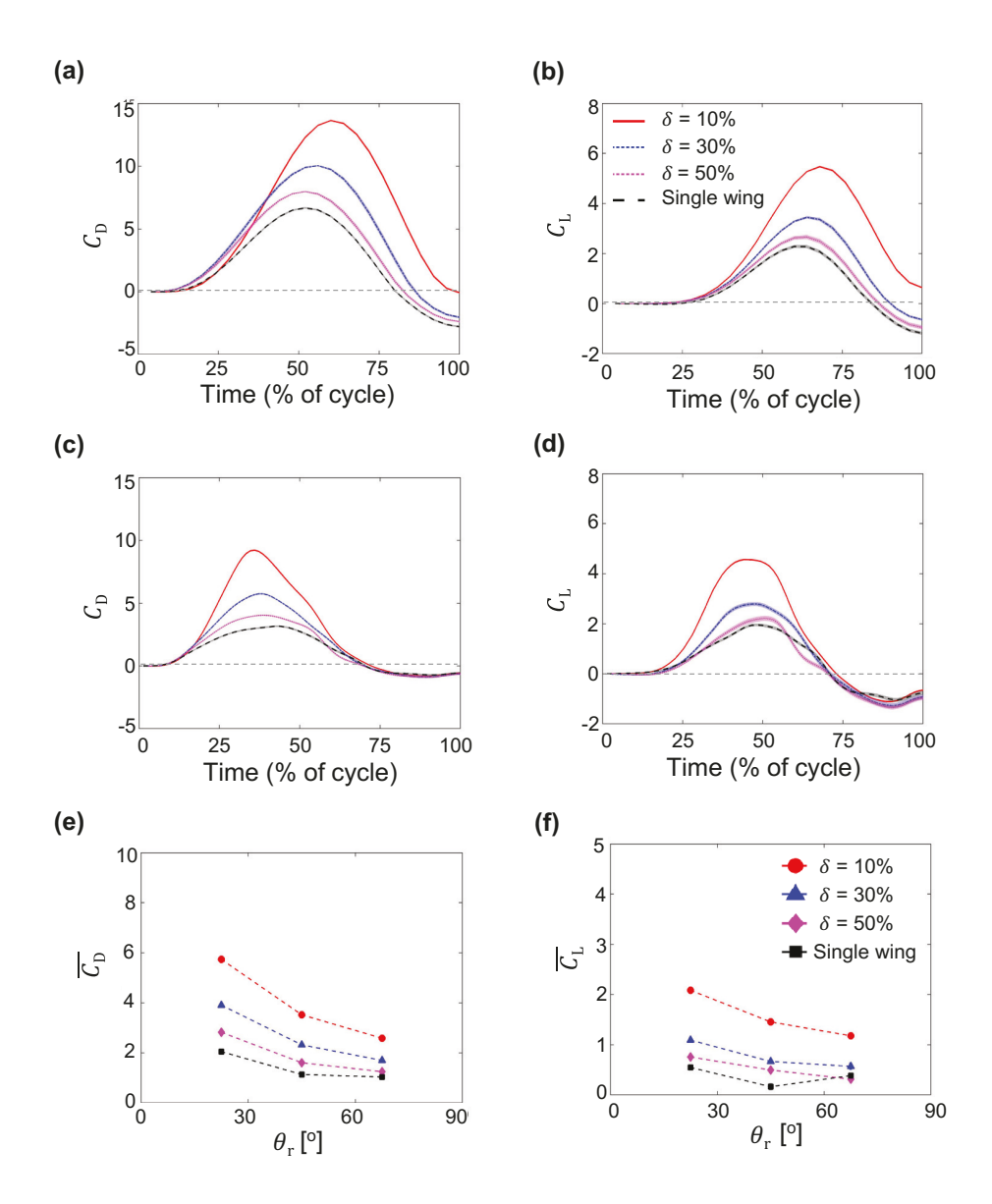


FIG. 4. Force coefficients during bristled wing rotation at Re=10. Shading around each curve represents ± 1 standard deviation (SD) across 30 cycles. (a) and (b) show time-variation of drag coefficient (C_D) and lift coefficient (C_L), respectively, for $\theta_r = 22.5^\circ$. (c) and (d) show time-variation of C_D and C_L , respectively, for $\theta_r = 67.5^\circ$. (e) and (f) show cycle-averaged drag coefficient (C_D) and cycle-averaged lift coefficient (C_L), respectively, for varying θ_r . Legend for (a)-(d) is shown in (b); legend for (e)-(f) is shown in (f). The y-axis range for (a) and (c) is -5 to 15, (b) and (d) is -2 to 8, (e) is 0 to 10 and (f) is 0 to 5.

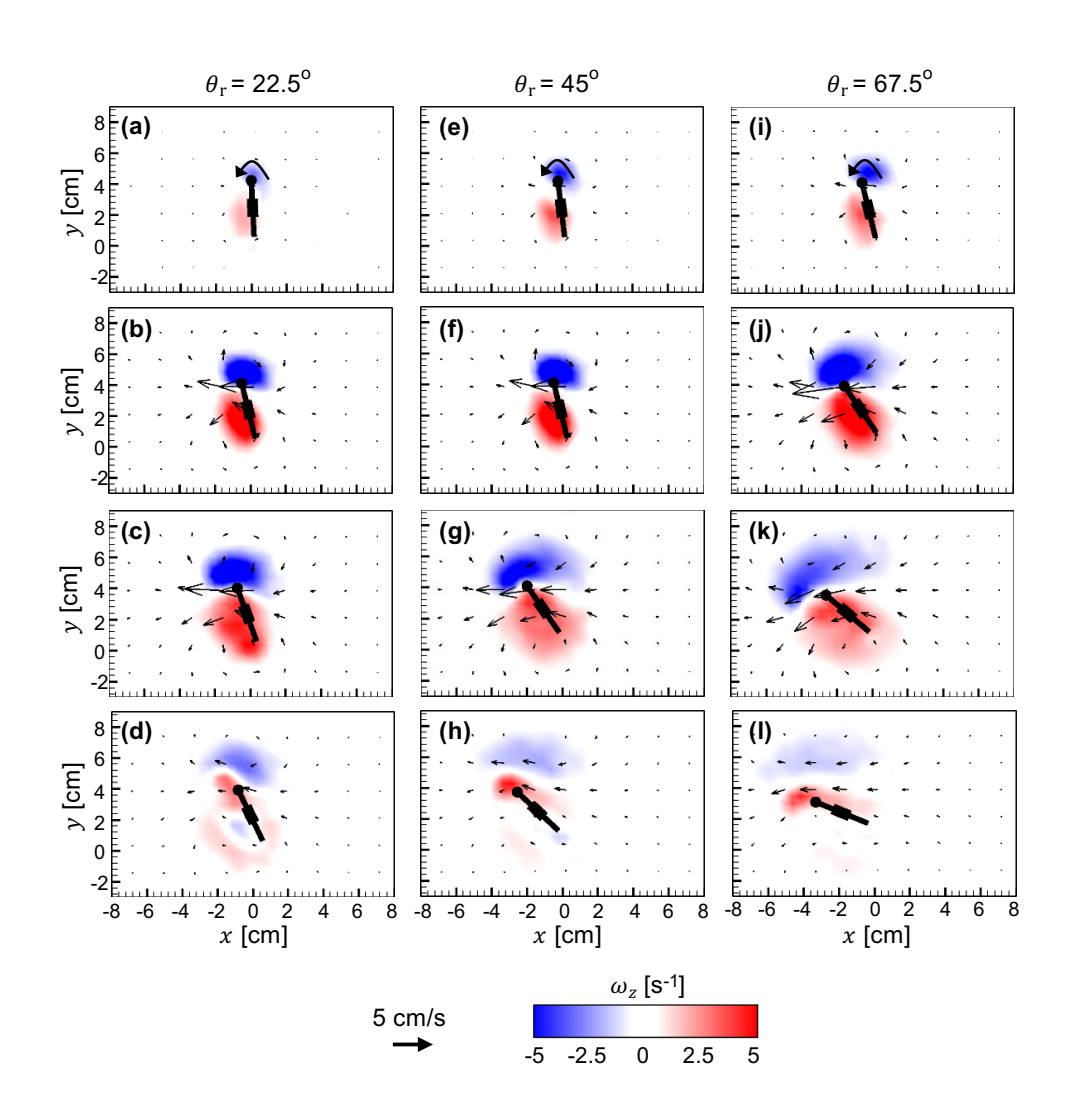


FIG. 5. Velocity vectors overlaid on out-of-plane *z*-vorticity (ω_z) contours for a single bristled wing in rotation at Re=10. (a)-(d) $\theta_r=22.5^\circ$; (e)-(h) $\theta_r=45^\circ$; (i)-(l) $\theta_r=67.5^\circ$. For each θ_r , 4 timepoints (25%, 50%, 75% and 100% of cycle time) are shown along each column ((a)-(d); (e)-(h); (i)-(l)) from top to bottom.

294 (d)) to 50% (**Figure 6(e)-(h)**) diffused the vorticity in both the LEV and TEV. Relative to the LEV for each δ , we observed a weaker TEV (i.e., smaller ω_z) for δ =10% as compared to δ =50% (**Figure 6(a)-(d)**). The LEV of the bristled wing pair was stronger and smaller in size for smaller δ compared to the LEV of bristled wing with larger δ (**Figure 6(e)-(h)**) that was weaker and more diffused. Similar to the single wing, LEV and TEV of the bristled wing pair for both δ =10% and 50% was found to increase in size with increasing cycle duration (T) before dissipating at the end of the cycle (100%T).

Similar to the observations at θ_r =22.5°, increasing δ diffused and decreased the strength of both the LEV and TEV when the bristled wing pair was rotated to θ_r = 67.5° (compare **Figure 6(i)-(l)**

and **Figure 6(m)-(p)**). In contrast to $\theta_r = 22.5^\circ$ where LEV and TEV were found to increase in strength from 50%T to 75%T (**Figure 6(b),(c)**), we observed a drop in strength of both the LEV and TEV for $\theta_r = 67.5^\circ$ for both $\delta=10\%$ and 50% (**Figure 6(j),(k)**).

Pressure distribution. Positive and negative pressure regions were observed below (i.e., front surface of the wing that first encounters fluid during rotation) and above (back surface of the wing)
the single bristled wing in rotation, respectively (**Figure 7**). Time-variation of pressure distribution around the single rotating wing was similar for all θ_r conditions (22.5°,45°,67.5°). Interestingly, we observed the pressure distribution in all θ_r conditions to approach zero at 75%T(**Figure 7(c),(g),(k)**), which corresponds to right after the start of wing deceleration. In addition,

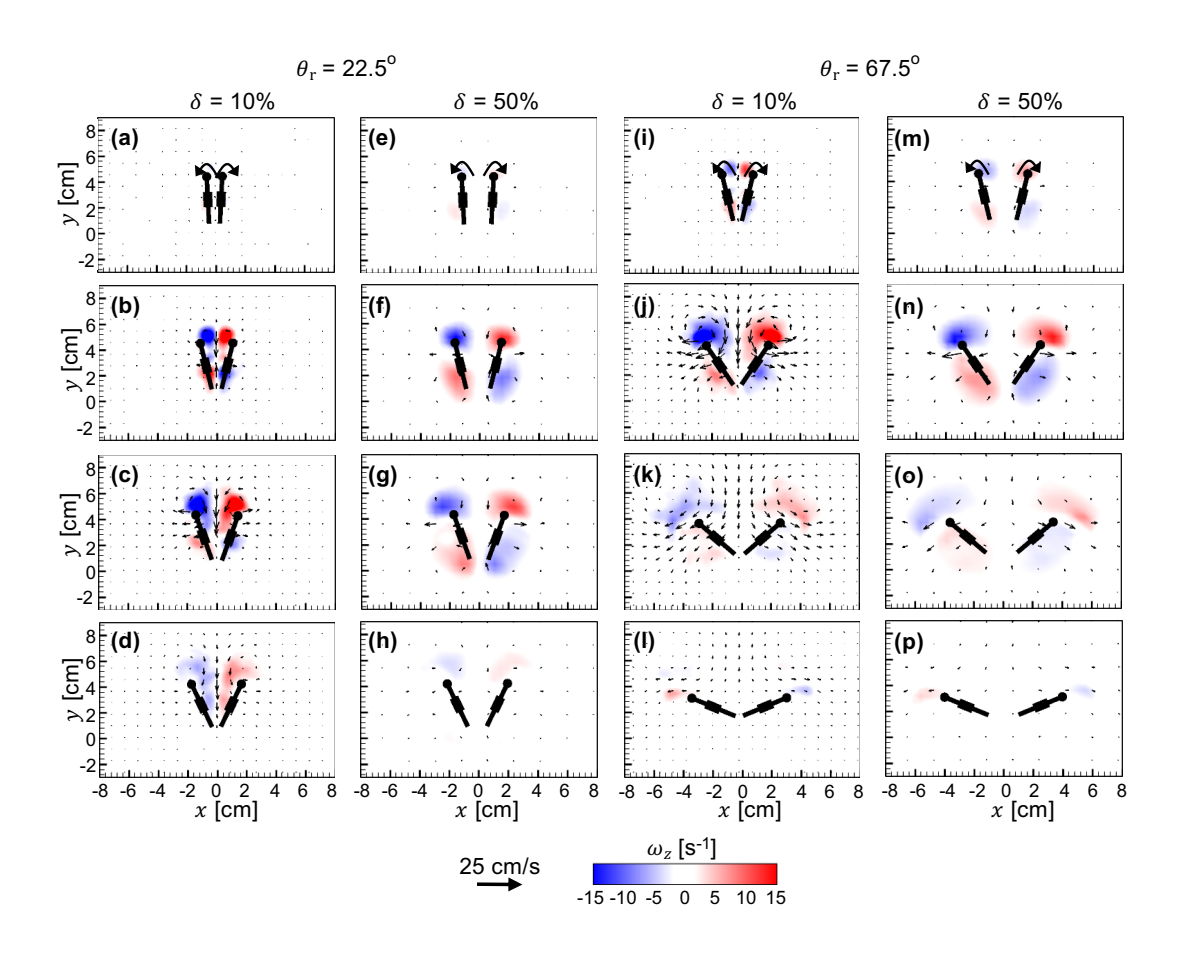


FIG. 6. Velocity vectors overlaid on out-of-plane *z*-vorticity (ω_z) contours for a bristled wing pair in rotation at Re=10. $\theta_r=22.5^\circ$ is shown for $\delta=10\%$ in (a)-(d) and for $\delta=50\%$ in (e)-(h). $\theta_r=67.5^\circ$ is shown for $\delta=10\%$ in (i)-(l) and for $\delta=50\%$ in (m)-(p). For each θ_r , 4 timepoints (25%, 50%, 75% and 100% of cycle time) are shown along each column ((a)-(d); (e)-(h); (i)-(l); (m)-(p)) from top to bottom.

ure $7(\mathbf{d})$,(\mathbf{h}),(\mathbf{l})), so that the positive pressure region was located above the wing and negative pressure region was located below the wing. This pressure reversal was particularly pronounced for the smallest θ_r =22.5° (**Figure 7(d**)). At 50%T, we observed the pressure distribution to be more diffused for the smallest θ_r =22.5° (**Figure 7(b**)) as compared to θ_r =67.5° (**Figure 7(j**)).

Pressure distribution around a bristle wing pair in rotation (**Figure 8**) was found to be completely different as compared to that of a rotating single wing (**Figure 7**). During the initial stages
portion of rotational motion, a diffused negative pressure region was observed near the LEs, just above

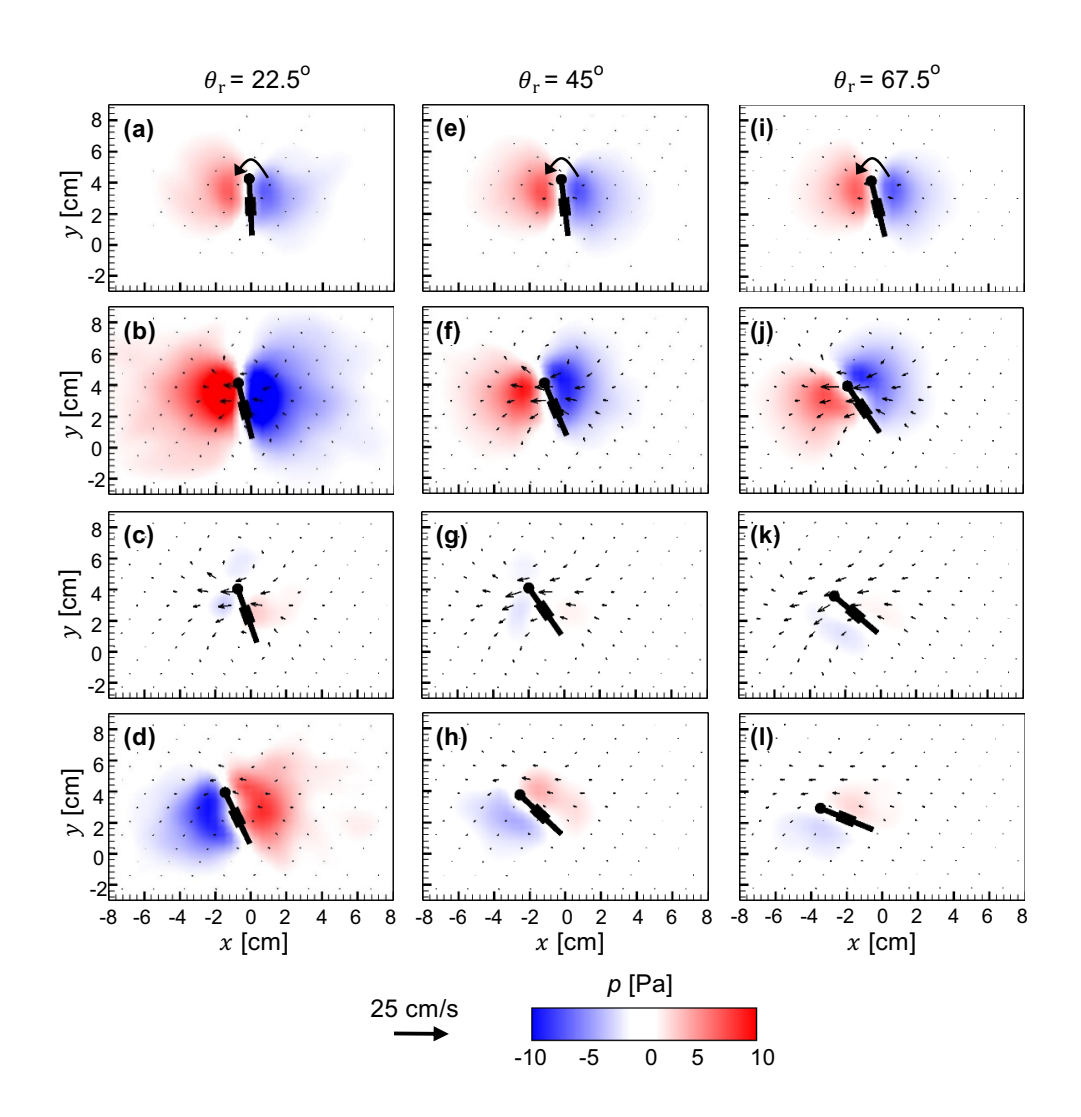


FIG. 7. Velocity vectors overlaid on pressure (p) contours for a single bristled wing in rotation at Re=10. (a)-(d) $\theta_r=22.5^\circ$; (e)-(h) $\theta_r=45^\circ$; (i)-(l) $\theta_r=67.5^\circ$. For each θ_r , 4 timepoints (25%, 50%, 75% and 100% of cycle time) are shown along each column ((a)-(d); (e)-(h); (i)-(l)) from top to bottom. Pressure distribution was calculated from measured velocity fields using the algorithm developed by Dabiri et al.³⁸

see the 'cavity' (i.e., inter-wing space) between the two wings (**Figure 8(a),(e),(i),(m)**). A weaker negative pressure region was also observed near the TEs, just below the cavity between the two wings. In addition, a diffused region of positive pressure was observed below each wing. For $\delta = 10\%$ and $\theta_r = 22.5^\circ$, we observed a diffused region of positive pressure to be distributed in the cavity between the wing pair at $\delta = 10\%$ (**Figure 8(b)**). The magnitude of positive pressure in the cavity decreased with increasing cycle time. Similar to the single wing model, we observed the positive and negative pressure regions to flip positions at the end of the cycle (100% 7; **Figure 8(d),(h),(l),(p)**). Increasing δ to $\delta = 10\%$ reduced the positive pressure between the wings and simultaneously increased the magnitude of negative pressure near the TEs (compare **Figure 8(b)**) and **Figure 8(f)**). At $\delta = 10\%$ (**Figure 8(c)**), we found both the positive and negative pressure distribution around the wings to substantially decrease in strength.

Time-variation of pressure distribution around a bristled wing pair rotated to θ_r =67.5° resembled that of θ_r =22.5°. However, the positive pressure region in the cavity between the wings for δ =10% and θ_r =22.5° (**Figure 8(b)**) was essentially absent for δ =10% and θ_r =67.5° (**Figure 8(j)**).

Increasing θ_r to 67.5° allowed the negative pressure region near the LEs (above the cavity) to diffuse over a larger region as compared to θ_r =22.5°. In contrast to increasing δ for θ_r =22.5°

(**Figure 8(f)**), increasing δ for θ_r =67.5° resulted in negative pressure distribution in the cavity between the wing at 50% cycle time (**Figure 8(n)**). Enhanced viscous diffusion of vorticity was observed for $Re \sim \mathcal{O}(10)$ in a previous study²⁰ of a solid elliptical wing (similar aspect ratio as the wings used in this study), undergoing constant velocity revolution at a fixed angle of attack. As the two wings of a bristled wing pair in rotation are in close proximity throughout a cycle (especially for θ_r =22.5° at δ =10%), we speculate that positive pressure is diffused from outside the wings to within the cavity between the wings via the inter-bristle gaps.

343 B. Bristled wings in linear translation

Aerodynamic force generation. In general, both C_L and C_D were observed to follow similar trends throughout a cycle (**Figure 9**). For all translational angles (θ_t) that were tested, we observed an increase in C_L and C_D during translational acceleration (see **Figure 3**(a) for prescribed translation motion profile), followed by C_L and C_D remaining approximately constant during constant velocity translation, and a subsequent drop in C_L and C_D during translational deceleration (**Figure 9**(a),(b)). When θ_t was increased from 22.5° to 67.5°, we observed large reduction in C_D compared to the

small reduction in C_L (compare (**Figure 9(a),(b)**) and **Figure 9(c),(d)**). In addition, increasing θ_t decreased peak values of C_L and C_D during translational acceleration by a larger extent as compared to reduction in peak coefficients during constant velocity translation. Similar to wing rotation, we observed C_D and C_L to drop below zero toward the end of the cycle for θ =22.5° (**Figure 9(a),(b)**). A noticeable drop in C_D and C_L was observed with increasing δ for θ_t =22.5°. Increasing θ_t to 67.5° decreased the drop in C_D and C_L that was observed with increasing δ . Interestingly, changing δ was found to affect C_D and C_L mostly during translational acceleration when the wings were closer to each other, promoting wing-wing interaction. After translational acceleration, when the wings translated further apart, C_L and C_D of the bristled wing pair for all δ values were similar to those generated by a single translating wing.

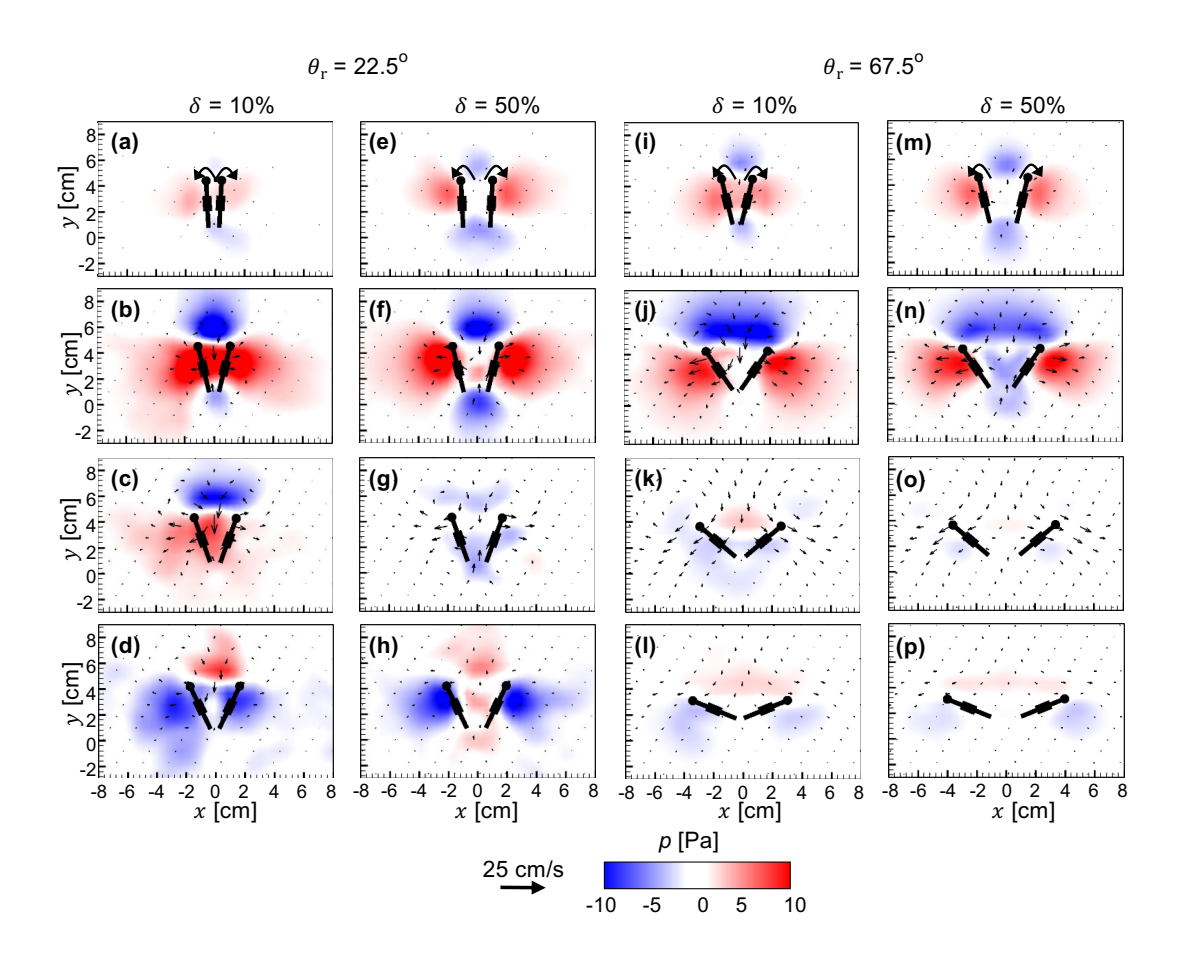


FIG. 8. Velocity vectors overlaid on pressure (p) contours for a bristled wing pair in rotation at Re=10. $\theta_r=22.5^\circ$ is shown for $\delta=10\%$ in (a)-(d) and for $\delta=50\%$ in (e)-(h). $\theta_r=67.5^\circ$ is shown for $\delta=10\%$ in (i)-(l) and for $\delta=50\%$ in (m)-(p). For each θ_r , 4 timepoints (25%, 50%, 75% and 100% of cycle time) are shown along each column ((a)-(d); (e)-(h); (i)-(l); (m)-(p)) from top to bottom.

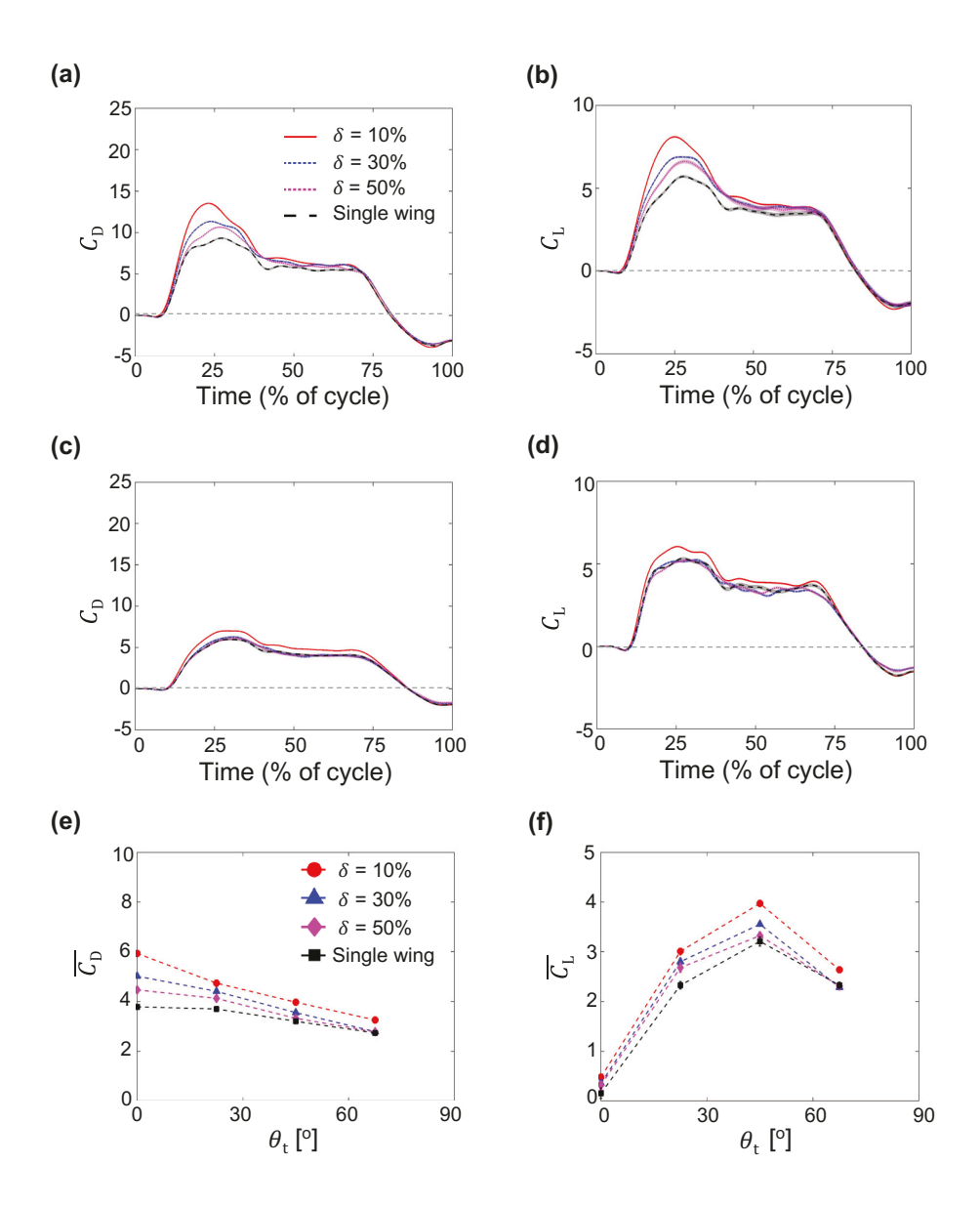


FIG. 9. Force coefficients during linear translation of bristled wings at Re=10. Shading around each curve represents ± 1 SD across 30 cycles. (a) and (b) show time-variation of C_D and C_L , respectively, for $\theta_t=22.5^\circ$. (c) and (d) show time-variation of C_D and C_L , respectively, for $\theta_t=67.5^\circ$. (e) and (f) show cycle-averaged coefficients $\overline{C_D}$ and $\overline{C_L}$, respectively, for varying θ_t . Legend for (b)-(d) is shown in (a); legend for (f) is shown in (e). The y-axis range for (a) and (c) is -5 to 25, (b) and (d) is -5 to 10, (e) is 0 to 10 and (f) is 0 to 5.

 $\overline{C_D}$ decreased with increasing θ_t , and increasing δ also resulted in decreasing $\overline{C_D}$ for lower values of θ_t . $\overline{C_D}$ was mostly independent of δ for $\theta_t \geq 45^\circ$, suggesting that increasing θ_t reduces wing-wing interaction. In sharp contrast to $\overline{C_D}$, $\overline{C_L}$ increased with increasing θ_t until 45° and subsequently decreased for θ_t =67.5° (**Figure 9(f)**). This suggests substantial changes in flow field likely occur for 45° $< \theta_t \leq 67.5^\circ$ to reduce $\overline{C_L}$ in this range. In addition, increasing δ resulted in smaller changes in $\overline{C_L}$ as compared to changes in $\overline{C_D}$.

Vorticity distribution. A single bristled wing in linear translation produced counter-rotating vortices at the LE and TE (**Figure 10**). Across all θ_t values, we observed a LEV and a TEV that were attached to the wing, and their strength increased in time before dissipating at the end of the cycle (100%T). Also, increasing θ_t decreased the strength of both the LEV and TEV during early translation (**Figure 10(a),(e),(i),(m)**). Minimal variation was observed in the vorticity magnitudes of LEV and TEV cores from 50%T to 75%T across all θ_t values.

For a bristled wing pair in linear translation at θ_t =22.5°, increasing δ from 10% to 50% degreesed the strength of both the LEV and TEV (compare **Figure 11(a)-(d)** and **Figure 11(e)-(h)**). However, at the end of cycle, vorticity distribution around each wing of the bristled wing pair was similar to that of a single wing in linear translation (compare **Figure 10(h)** and **Figure 11(d),(h)**). Similar to the single bristled wing in linear translation, we observed minimal variation in the vorticity magnitudes of the LEV and TEV from 50%T to 75%T (**Figure 11(b),(c),(f),(g)**). Similarly, for the bristled wing pair in linear translation at θ_t =67.5°, increasing δ decreased the strength of both the LEV and TEV (compare **Figure 11(i)-(l)** and **Figure 11(m)-(p)**). In contrast to θ_t = 380 22.5°, LEV and TEV strength for θ_t =67.5° showed larger variation with increasing δ throughout the cycle.

Pressure distribution. Similar to a single rotating wing, a single bristled wing undergoing linear translation showed positive and negative pressure regions below and above the wing, respectively (Figure 12). Time-variation of pressure distribution around the single translating wing was similar for all θ_t conditions. Increasing θ_t weakened the pressure distribution throughout the cycle. In addition, pressure distribution around the wing flipped in sign at the end of the translation (100%T). This pressure reversal was more pronounced for smaller θ_t ($\leq 22.5^{\circ}$).

Pressure distribution around a bristle wing pair in linear translation (**Figure 13**) was found to be different compared to that of a translating single wing (**Figure 12**) mostly at the start of the cycle on account of wing-wing interaction. During initial stages of linear translation, a diffused negative pressure region was observed near the LEs just above the cavity between the wings and

per near the TEs (**Figure 13(a),(e),(i),(m)**). Also, a diffused region of positive pressure was observed below each wing. For $\delta = 10\%$ and $\theta_t = 22.5^\circ$, we observed a diffused region of negative pressure to be distributed in the cavity between the wing pair and near the LE at 50%T (**Figure 13(b)**). This is in contrast to the positive pressure region that was observed between the wing pair at the same time point during rotation to $\theta_r = 22.5^\circ$ (**Figure 8(b)**). As the wing translates in time, the negative pressure build up in between the wings likely occurs due to increasing inter-wing separation that is not conducive for wing-wing interaction. Similar to the single translating wing, we observed the positive and negative pressure regions to flip positions at the end of the cycle (100%T; **Figure 13(d),(h),(l),(p)**). Increasing δ to 50% for $\theta_t = 22.5^\circ$ reduced the negative pressure between the wings (compare **Figure 13(b)** and **Figure 13(f)**). From $\sim 50\%T$ onward for $\theta_t = 22.5^\circ$, we found both the positive and negative pressure distribution around the wing to be mostly unaffected with

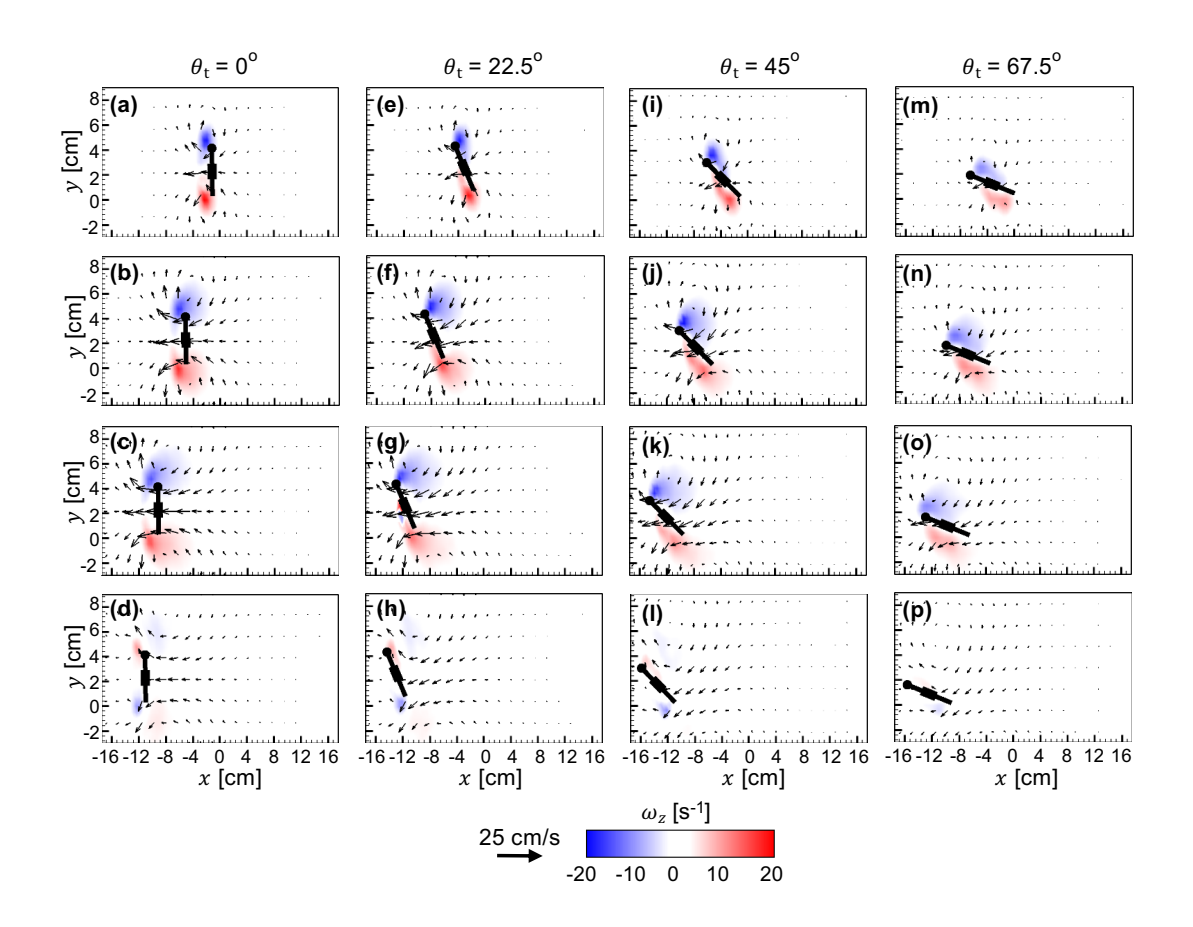


FIG. 10. Velocity vectors overlaid on out-of-plane *z*-vorticity (ω_z) contours for a single bristled wing in linear translation at Re=10. (a)-(d) $\theta_t=0^\circ$; (e)-(h) $\theta_t=22.5^\circ$; (i)-(l) $\theta_t=45^\circ$; (m)-(p) $\theta_t=67.5^\circ$. For each θ_t , 4 timepoints (25%, 50%, 75% and 100% of cycle time) are shown along each column ((a)-(d); (e)-(h); (i)-(l); (m)-(p)) from top to bottom.

403 increasing δ .

In contrast to θ_t =22.5°, linear translation of the bristled wing pair at θ_t =67.5° showed minimal change in pressure distribution when comparing identical time points at δ =10% (**Figure 13(i)**-406 (**I**)) and δ =50% (**Figure 13(m)**-(**p**)). This suggests that there is a limit to θ_t after which wingwing interaction is unaltered for $\delta \geq$ 10%. Just after the start of translation at θ_t =67.5°, we found negative pressure to be distributed in between the wing and positive pressure below the wings for both δ =10% and 50%. The magnitudes of negative and positive pressures at θ_t =67.5° were found to be substantially lower than those of θ_t =22.5° throughout the cycle.

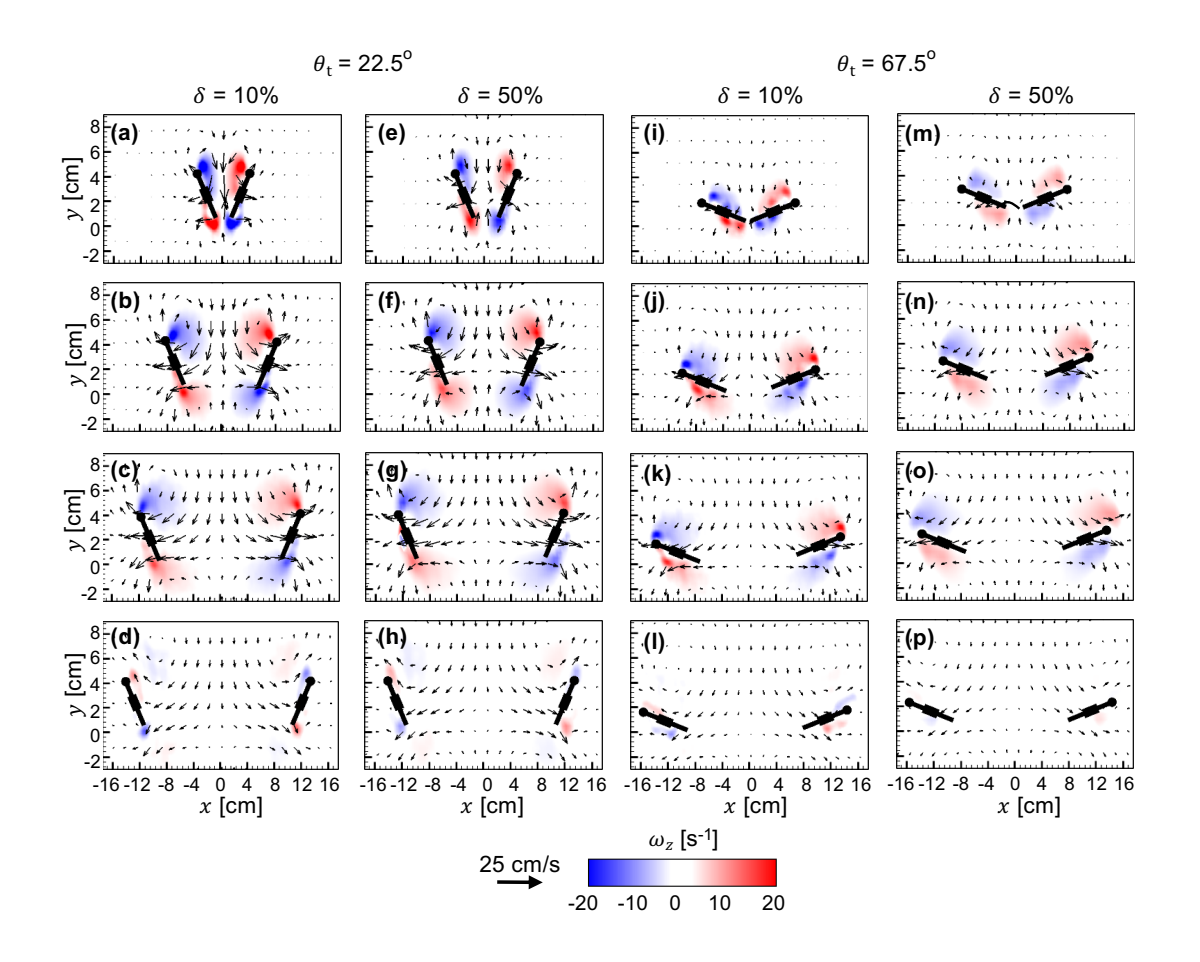


FIG. 11. Velocity vectors overlaid on out-of-plane *z*-vorticity (ω_z) contours for a bristled wing pair in linear translation at Re=10. $\theta_t=22.5^\circ$ is shown for $\delta=10\%$ in (a)-(d) and for $\delta=50\%$ in (e)-(h). $\theta_t=67.5^\circ$ is shown for $\delta=10\%$ in (i)-(l) and for $\delta=50\%$ in (m)-(p). For each θ_t , 4 timepoints (25%, 50%, 75% and 100% of cycle time) are shown along each column ((a)-(d); (e)-(h); (i)-(l); (m)-(p)) from top to bottom.

411 C. Bristled wings during combined rotation and linear translation

At ζ =25%, both C_L and C_D were found to peak at two timepoints in the cycle (**Figure 14(a),(b)**). One of the timepoints correspond to where the rotational wing motion reached peak velocity and other time point correspond to the peak translational velocity. With increase in ζ to 100% (**Figure 14 (c),(d)**), we observed both C_L and C_D to peak at only one time point early in the cycle. In addition, peak values of C_L and C_D increased with increasing ζ . For each ζ , increasing δ decreased peak values of both C_L and C_D . However, during wing translation following overlapping motion, both C_L and C_D showed minimal variation for varying δ . Similar to linear translation, both C_L and C_D dropped below zero close towards the end of the cycle.

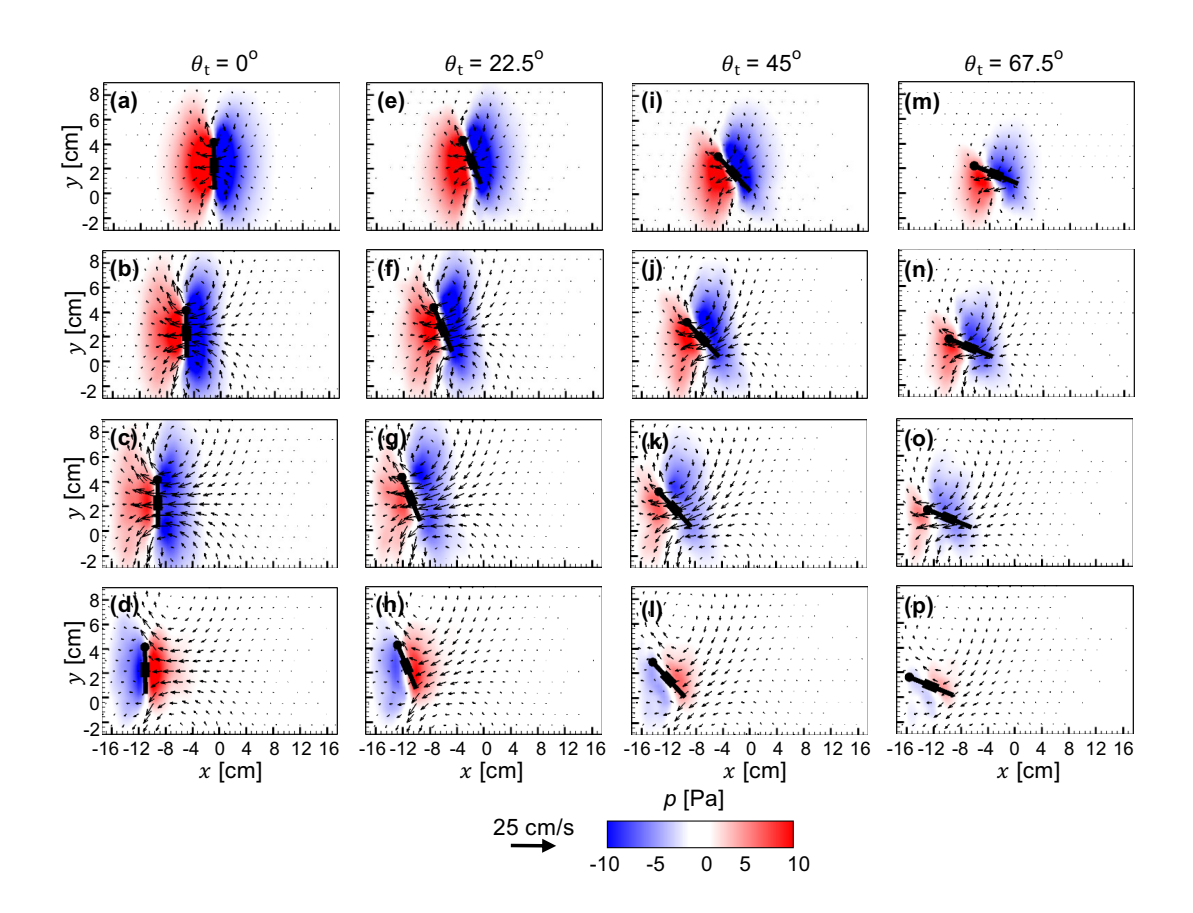


FIG. 12. Velocity vectors overlaid on pressure (p) contours for a single bristled wing in linear translation at Re=10. (a)-(d) $\theta_r=0^\circ$; (e)-(h) $\theta_r=22.5^\circ$; (i)-(l) $\theta_r=45^\circ$; (m)-(p) $\theta_t=67.5^\circ$. For each θ_t , 4 timepoints (25%, 50%, 75% and 100% of cycle time) are shown along each column ((a)-(d); (e)-(h); (i)-(l); (m)-(p)) from top to bottom.

In general, cycle-averaged coefficients ($\overline{C_D}$ and $\overline{C_L}$, **Figure 14(e),(f)**) were observed to increase with increasing ζ . Increasing δ decreased both $\overline{C_D}$ and $\overline{C_L}$. The extent of $\overline{C_L}$ variation with ζ was substantially smaller than that of $\overline{C_D}$.

Vorticity distribution. Figure 15 shows the flow generated by a single bristled wing performing combined rotation and linear translation. With increasing ζ , the strength of both LEV and TEV were found to increase during early stages of wing motion (25%T) This could likely be on account of both wings reaching rotational deceleration phase at 25%T for all ζ . At 75%T, the strength of both LEV and TEV were found to have little to no change with increasing ζ (Figure 14(c),(g),(k),(o)).

For a bristled wing pair performing combined rotation and linear translation at ζ =25% (**Fig**-

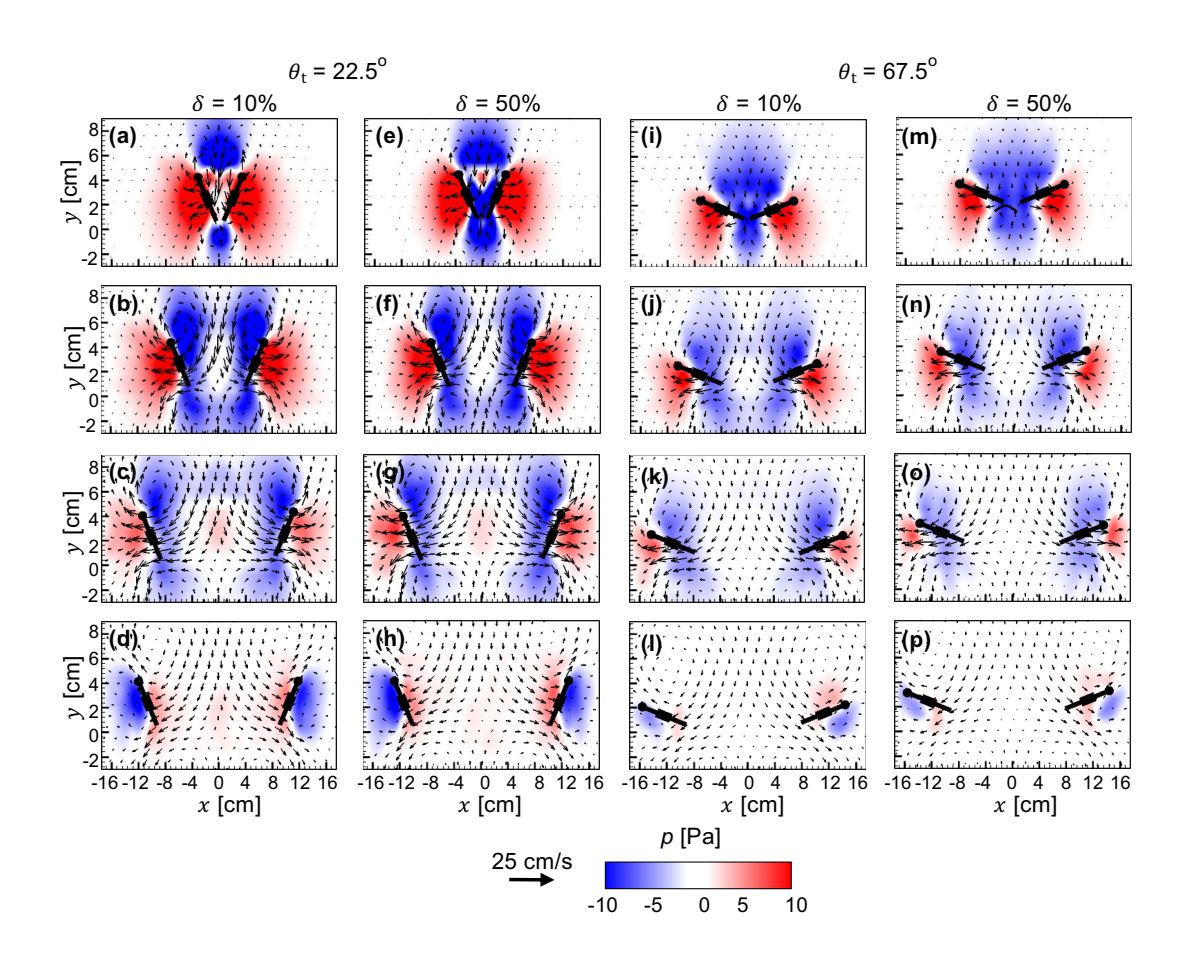


FIG. 13. Velocity vectors overlaid on pressure (p) contours for a bristled wing pair in linear translation at Re=10. $\theta_t=22.5^\circ$ is shown for $\delta=10\%$ in (a)-(d) and for $\delta=50\%$ in (e)-(h). $\theta_t=67.5^\circ$ is shown for $\delta=10\%$ in (i)-(l) and for $\delta=50\%$ in (m)-(p). For each θ_t , 4 timepoints (25%, 50%, 75% and 100% of cycle time) are shown along each column ((a)-(d); (e)-(h); (i)-(l); (m)-(p)) from top to bottom.

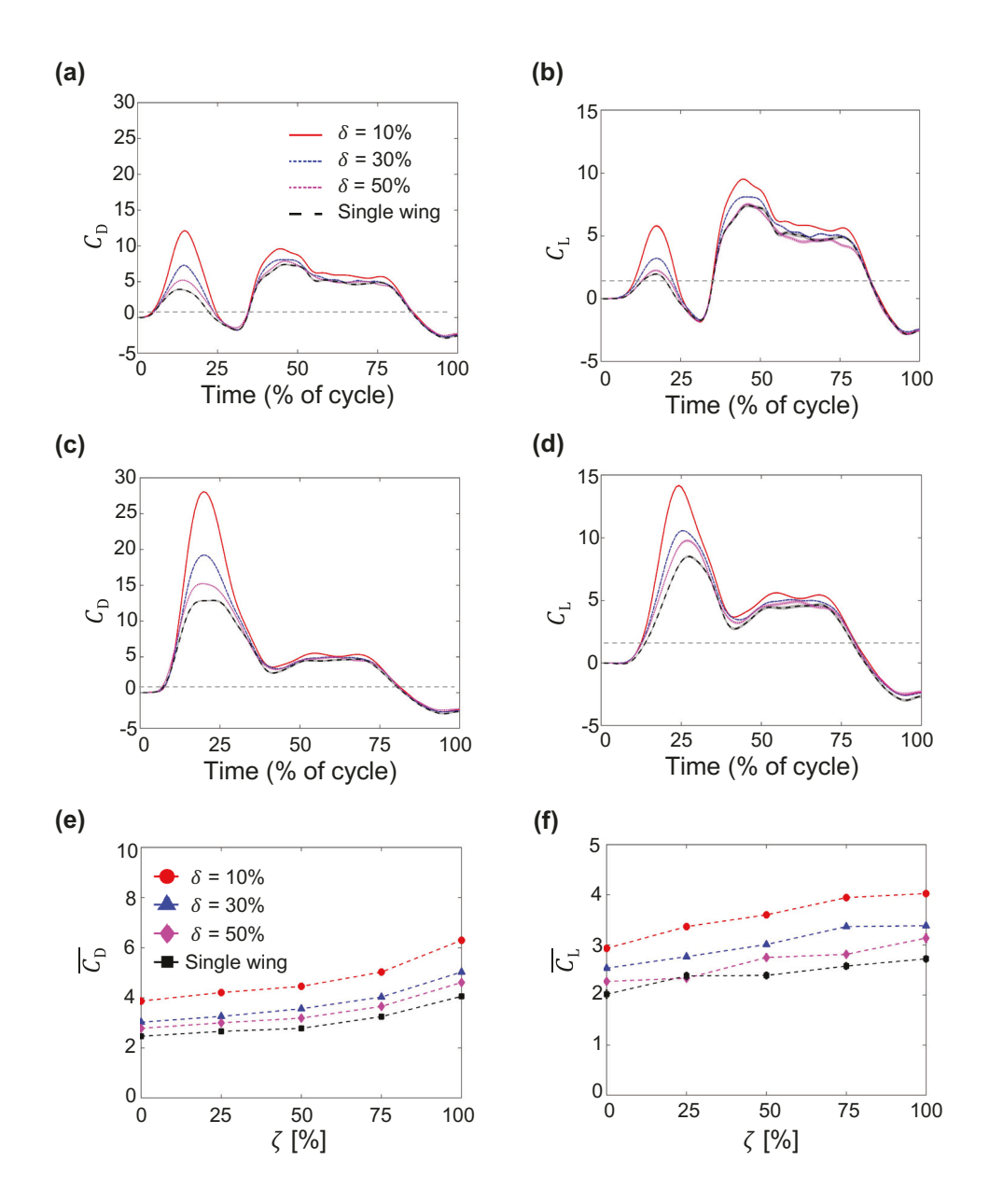


FIG. 14. Force coefficients during combined rotation and linear translation of bristled wings at Re=10. Shading around each curve represents ± 1 SD across 30 cycles. (a) and (b) show time-variation of $C_{\rm D}$ and $C_{\rm L}$, respectively, for overlap $\zeta=25\%$. (c) and (d) show time-variation of $C_{\rm D}$ and $C_{\rm L}$, respectively, for $\zeta=100\%$. (e) and (f) show cycle-averaged coefficients $\overline{C_{\rm D}}$ and $\overline{C_{\rm L}}$, respectively, for varying ζ . Legend for (b)-(d) is shown in (a); legend for (f) is shown in (e). The y-axis range for (a) and (c) is -5 to 30, (b) and (d) is -5 to 15, (e) is 0 to 10 and (f) is 0 to 5.

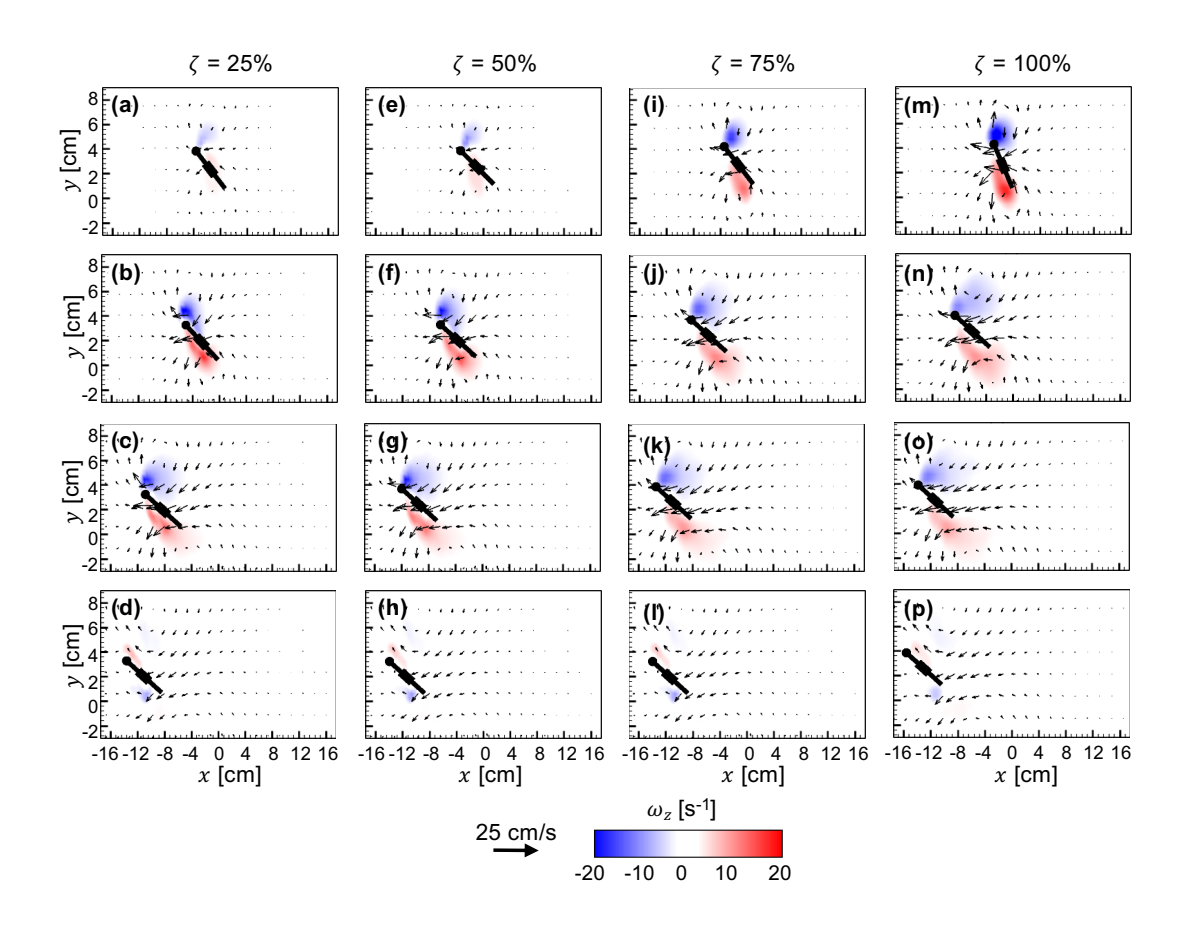


FIG. 15. Velocity vectors overlaid on out-of-plane z-vorticity (ω_z) contours for combined rotation and linear translation of a single bristled wing at Re=10. (a)-(d) $\zeta=25\%$; (e)-(h) $\zeta=50\%$; (i)-(l) $\zeta=75\%$; (m)-(p) $\zeta=100\%$. For each ζ , 4 timepoints (25%, 50%, 75% and 100% of cycle time) are shown along each column ((a)-(d); (e)-(h); (i)-(l); (m)-(p)) from top to bottom.

ure 16(a)-(h)), increasing δ decreased the strength of both the LEV and TEV during initial stages of wing motion (25%T and 50%T). Towards the end of cycle with increasing δ , there were essentially no changes to the vorticity of the LEV and TEV cores. Similar trends were also observed for ζ =100% (Figure 16(i)-(p)).

Similar to a single wing, increasing the overlap (ζ) for one particular initial inter-wing spacing (δ) increased the strength of both LEV and TEV at 25% and 50% of cycle time. However, LEV and TEV strength showed little to no variations towards the end of cycle time for $\zeta = 25\%$ and 100%.

Pressure distribution. A single bristled wing performing combined rotation and linear translation showed substantial changes in pressure distribution with changing ζ (Figure 17). Similar to vorticity distribution, both positive and negative pressure magnitudes increased with increasing

overlap during 25%T (Figure 17(a),(e),(i),(m)) and 50%T (Figure 17(b),(f),(j),(n)). At 75%T (Figure 17(c),(g),(k),(o)) and 100%T (Figure 17(d),(h),(l),(p)), increasing ζ resulted in little to 444 no changes to the pressure distribution around the wing.

Pressure distribution around a bristle wing pair (**Figure 18**) was found to be different compared to that of a single wing (both cases performing rotation and linear translation) mostly during early stages of the cycle, where wing-wing interaction appears to have the most influence. During the earlier part of the combined rotation and translation cycle at 50%T and $\zeta=25\%$ (**Figure 18(b),(f)**), we observed an increase in negative pressure distribution within the cavity between the wings and positive pressure distributed below each wing. With further increase in time from 75%T

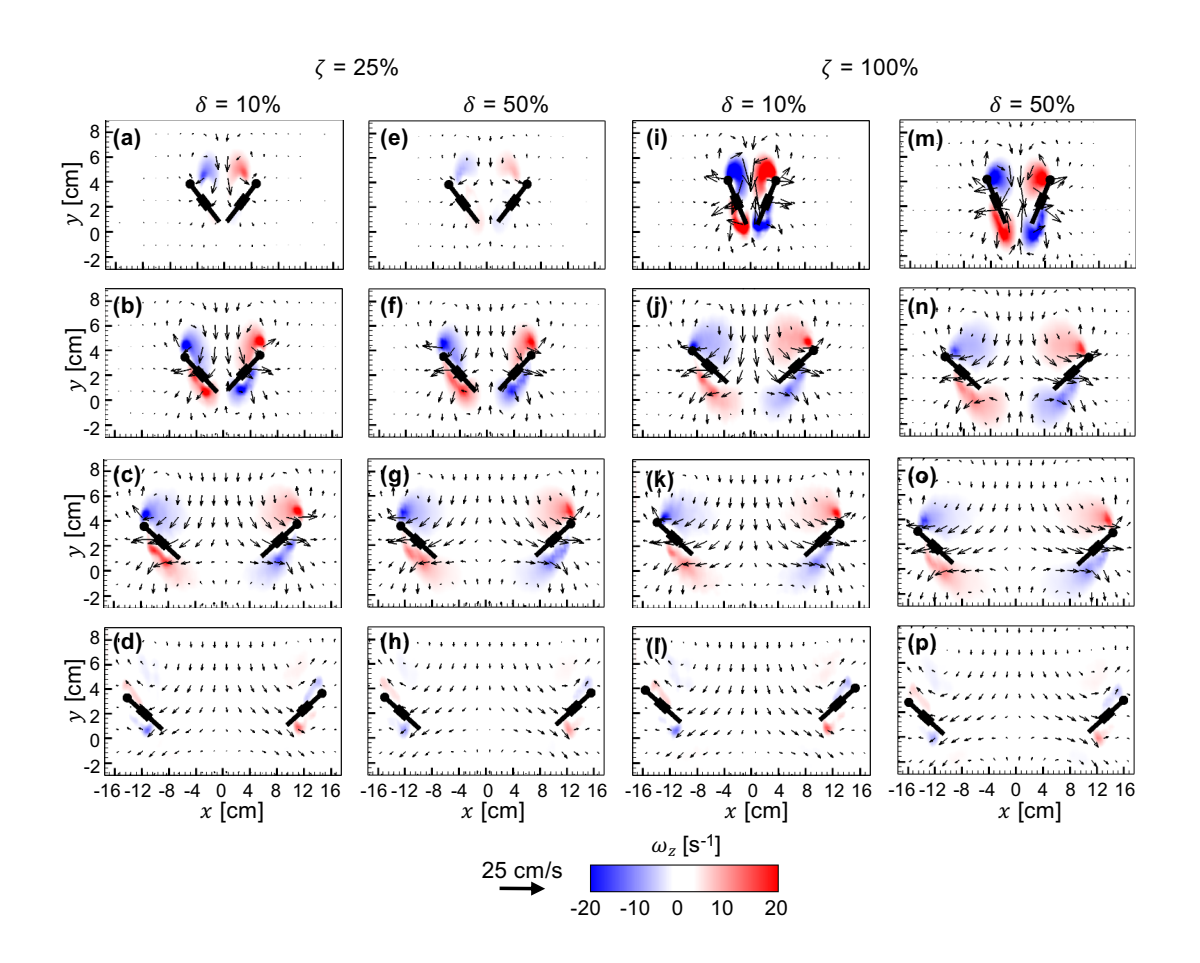


FIG. 16. Velocity vectors overlaid on out-of-plane *z*-vorticity (ω_z) contours for combined rotation and linear translation of a bristled wing pair at Re=10. $\zeta=25\%$ is shown for $\delta=10\%$ in (a)-(d) and for $\delta=50\%$ in (e)-(h). $\zeta=100\%$ is shown for $\delta=10\%$ in (i)-(l) and for $\delta=50\%$ in (m)-(p). For each ζ , 4 timepoints (25%, 50%, 75% and 100% of cycle time) are shown along each column ((a)-(d); (e)-(h); (i)-(l); (m)-(p)) from top to bottom.

(Figure 18(c),(g)) to 100%T (Figure 18(d),(h)), the pressure distribution starts to closely resemble that of a single wing, suggesting diminished influence of wing-wing interaction. Increasing δ at $\zeta = 25\%$ resulted in a drop in the pressure distribution only during the start of the cycle (25%T; Figure 18(a),(e)), and minimal variation in pressure distribution was observed between $\delta = 10\%$ (Figure 18(b)-(d)) and $\delta = 50\%$ (Figure 18(f)-(h)) for the remainder of the cycle.

Similar trends were observed with increasing δ for ζ =100% (**Figure 18(i)-(p)**) as compared to those discussed for ζ =25%. However, we observed the development of a strong negative pressure region in the cavity between the wings for δ =50% early into the cycle (25%T; **Figure 18(m)**). Also, larger negative and positive regions were observed for ζ =100% as compared to ζ =25%. However, we did not observe noticeable differences in the pressure distribution at 75%T and 100%T when changing either ζ or δ .

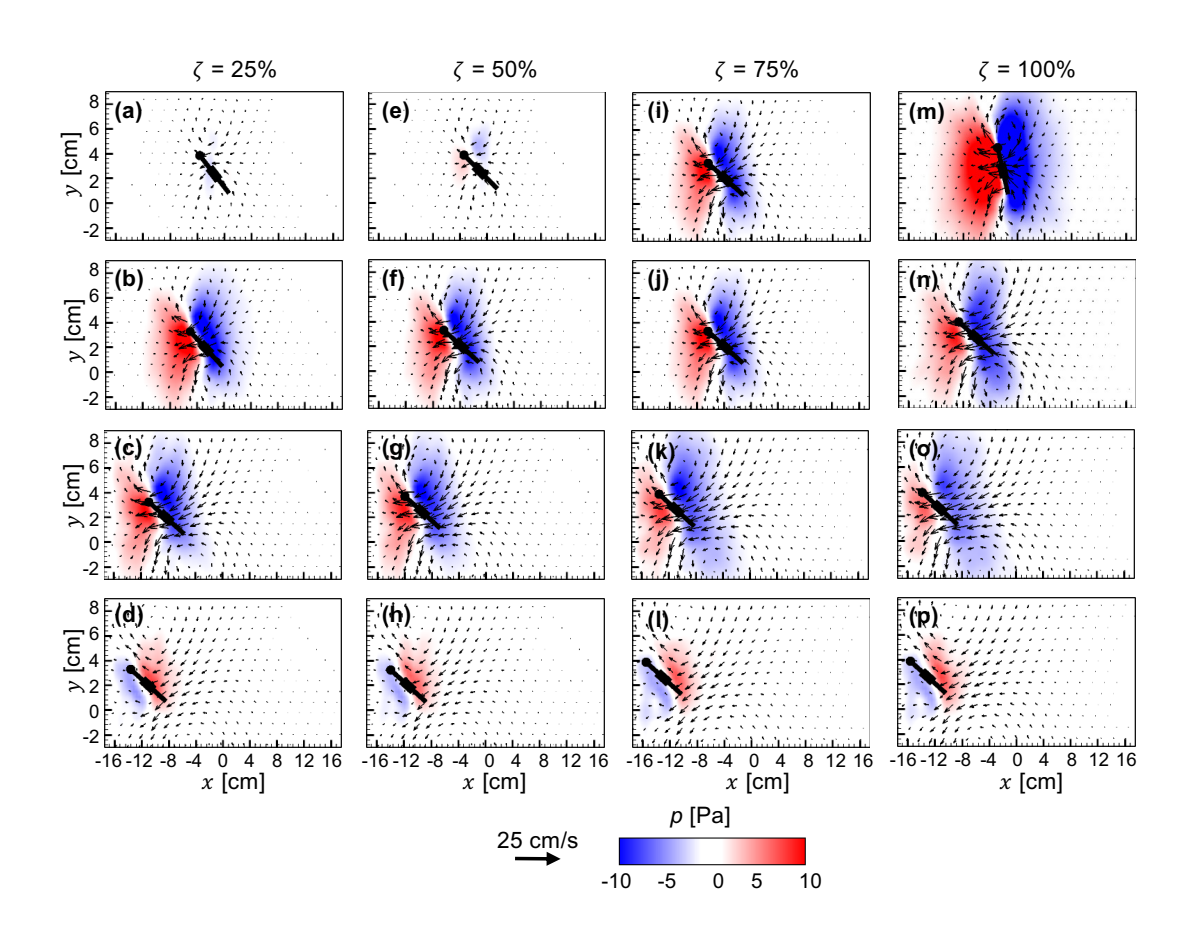


FIG. 17. Velocity vectors overlaid on pressure (p) contours for combined rotation and linear translation of a single bristled wing at Re=10. (a)-(d) $\zeta=25\%$; (e)-(h) $\zeta=50\%$; (i)-(l) $\zeta=75\%$; (m)-(p) $\zeta=100\%$. For each ζ , 4 timepoints (25%, 50%, 75% and 100% of cycle time) are shown along each column ((a)-(d); (e)-(h); (i)-(l); (m)-(p)) from top to bottom.

462 D. Reverse flow through bristled wings

Reverse flow capacity (RFC) by a bristled wing was quantified using the equation 13. RFC gives a dimensionless estimate of the capability of a given bristled wing model to leak fluid through the bristles on a bristled wing model for varying δ , θ_t , θ_r , and ζ (Figure 19). For all θ_r , RFC was in the range of 0%-80% (**Figure 19(a),(b)**). RFC was larger for smaller θ_r of 22.5° as compared to 67.5° at the same % of cycle time. In addition, having the wings closer (δ =10%) showed higher RFC for θ_r =22.5°. This is in agreement with the results of Loudon et al.²⁶, where the presence of a wall near bristled appendages was observed to promote inter-bristle flow. This increase in RFC can be attributed to net changes in pressure distribution around the wing for δ = 10% at θ_r =22.5°.

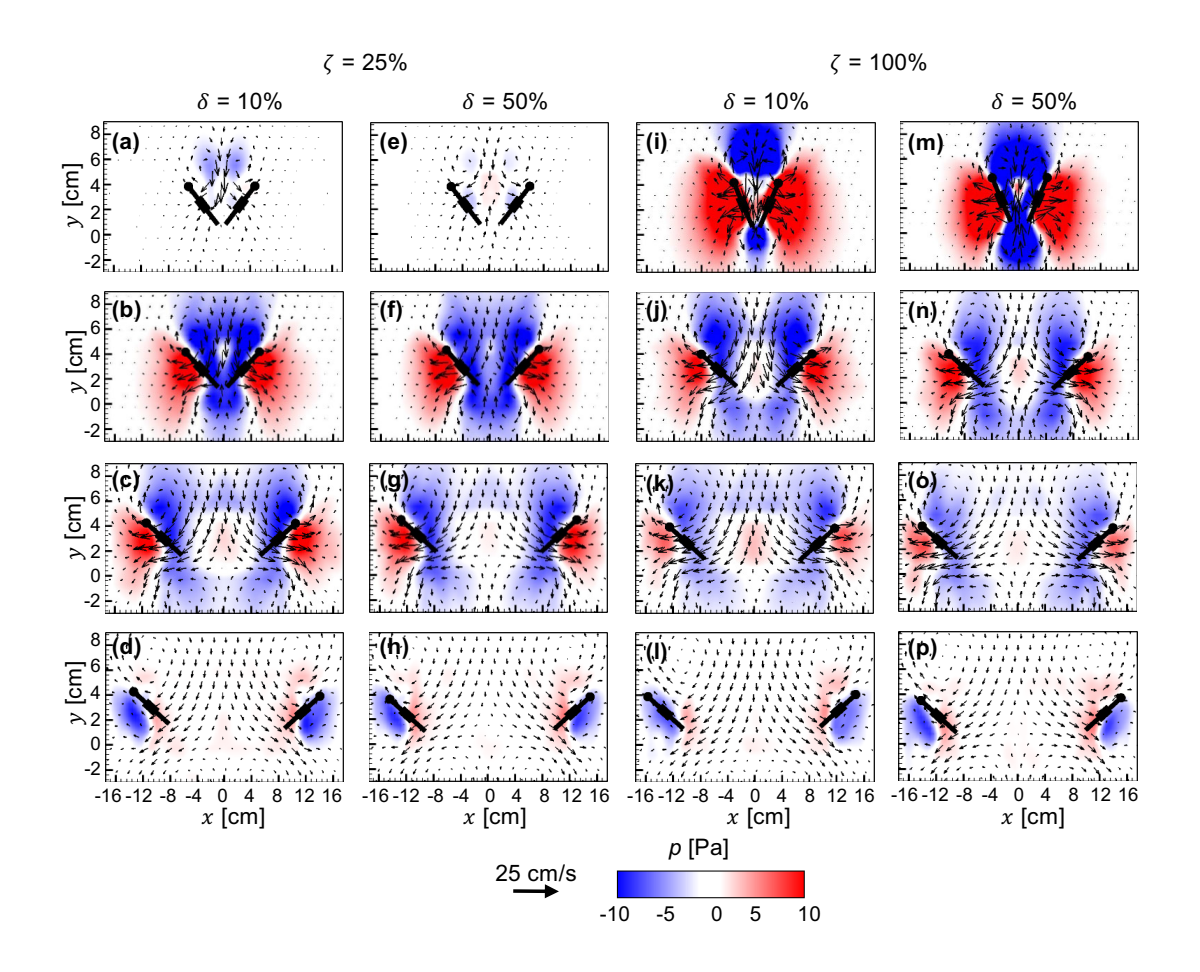


FIG. 18. Velocity vectors overlaid on pressure (p) contours for combined rotation and linear translation of a bristled wing pair at Re=10. $\zeta=25\%$ is shown for $\delta=10\%$ in (a)-(d) and for $\delta=50\%$ in (e)-(h). $\zeta=100\%$ is shown for $\delta=10\%$ in (i)-(l) and for $\delta=50\%$ in (m)-(p). For each θ_t , 4 timepoints (25%, 50%, 75% and 100% of cycle time) are shown along each column ((a)-(d); (e)-(h); (i)-(l); (m)-(p)) from top to bottom.

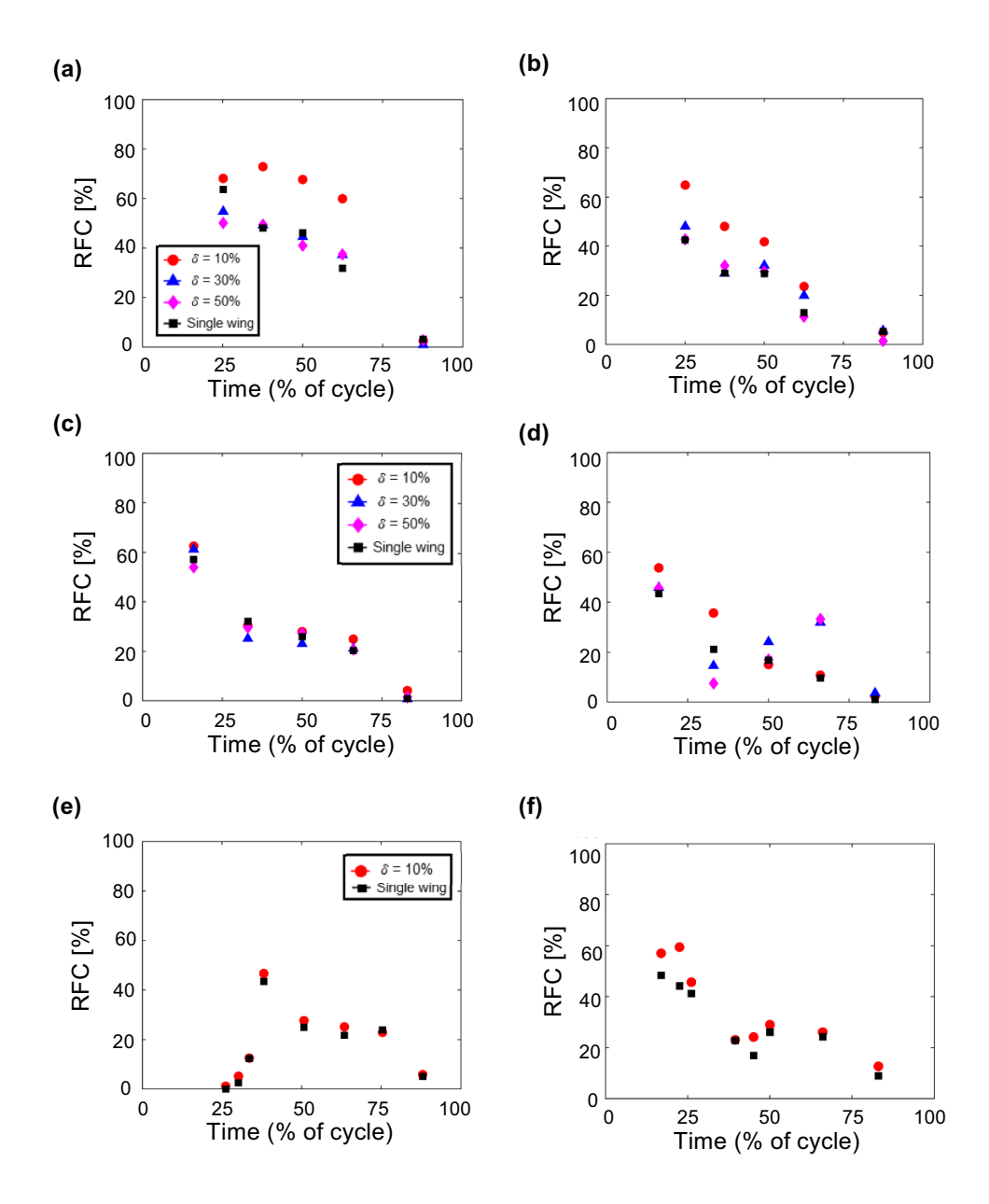


FIG. 19. Time-variation of reverse flow capacity (RFC), characterizing the reduction in volumetric flow of a bristled wing (or wing pair) with respect to a geometrically equivalent solid wing, as a function of δ and wing kinematics. (a) and (b) show RFC during rotation at θ_r =22.5° and θ_r =67.5°, respectively. (c) and (d) show RFC during linear translation at θ_t =22.5° and θ_t =67.5°, respectively. (e) and (f) show RFC during combined rotation and linear translation at ζ =25% and ζ =100%, respectively. Both single bristled wing and bristled wing pairs are included. See subsection II G for more details on definition and calculation of RFC.

Increasing δ beyond 10% showed little to no change in RFC. In addition, for changing θ_t (Figure 19(c),(d)) and ζ (Figure 19(e),(f)), we observe very little variation in RFC across all δ values. However, the RFC was found to change in time for each θ_t or ζ (in addition to θ_r). The latter suggests that RFC is largely dependent on wing kinematics and found to be more for smaller δ . Interestingly, higher values of RFC that were observed for lower θ_r and smaller δ were also associated with large C_D . While it is intuitive to expect that a bristled wing with larger capacity to leak flow through the bristles will reduce drag, this counter-intuitive finding suggests that the high drag forces were generated by formation of shear layers around the bristles as has been noted in previous studies 23,31.

480 IV. DISCUSSION

While several computational studies^{8,16–18,39} have examined wing-wing interaction in fling at 481 low Re for varying δ and ζ , the wings were modeled as solid wings unlike the bristled wings typically seen in tiny flying insects. Further, the few computational studies of wing-wing interaction of bristled wings^{7,22} did not isolate the specific roles of wing rotation from translation. We experimentally examined the flow structures and forces generated by a single bristled wing and a bristled wing pair under varying initial inter-wing distance (δ) at Re=10, for the following kinematics: rotation to θ_r about the TE, linear translation at a fixed angle θ_t , and combined rotation and linear translation (overlap duration ζ in %). The central findings for varying wing kinematics are: (1) increasing θ_r decreased both cycle-averaged lift $(\overline{C_L})$ and drag $(\overline{C_D})$ coefficients; (2) increasing θ_t 490 decreased $\overline{C_D}$ and approached $\overline{C_D}$ of a single wing at θ_t =67.5°; (3) $\overline{C_L}$ increased with increasing θ_t , peaking at θ_t =45° and decreasing thereafter at θ_t =45°; and (4) increasing ζ increased both $\overline{C_L}$ and $\overline{C_D}$. For all wing kinematics examined here, $\delta > 10\%$ resulted in smaller reduction of instantaneous lift coefficient $C_{\rm L}$ as compared to larger reduction of instantaneous drag coefficient $C_{\rm D}$. We find that peak $C_{\rm L}$ of a wing pair separated by δ =10% during rotation and during combined rotation and linear translation (ζ =25%) occurs close to the time point where an attached, asymmetric (in size) 496 LEV-TEV pair was observed over the wing. Finally, large values of C_D during rotation of a wing pair with δ =10% resulted from large positive pressure distribution between the wings.

498 A. Implications of vorticity distribution on lift force generation

Previous studies examining aerodynamic effects of varying δ of solid wing pairs 16,17,39 and 500 porous wing pairs 7 did not elaborate on the physical mechanism(s) responsible for lift augmentation observed with decreasing δ . A stable, attached TEV has been observed in addition to the 502 LEV for a single wing in revolution and in linear translation at $Re \le 32^{14,20}$, and this LEV-TEV vortical symmetry' has been identified as a primary reason for diminished lift generation at this 504 Re range 14 . Miller and Peskin 18 identified 'vortical asymmetry' (larger LEV, smaller TEV) during fling of a solid wing pair at $Re \le 32$ as the mechanism underlying the observed lift augmentation, 506 suggesting that wing-wing interaction can help recover some of the lift lost during the remainder of the cycle (latter attributed to 'vortical symmetry'). We examined circulation (Γ) of the LEV and TEV on a wing of the interacting bristled wing pair to explain the observed changes in lift generation under varying δ and kinematics (**Figure 20**).

Increasing θ_r from 22.5° to 67.5° increased the peak net circulation on the wing ($|\Gamma_{LEV}|$ - $|\Gamma_{TEV}|$) 510 ₅₁₁ by roughly 2.5 times for δ =10% (**Figure 20(a),(b)**). Surprisingly, we saw a drop in peak C_L with increasing θ_r (Figure 4(b),(d)). To examine the reason for this discrepancy, we calculated the spatially-averaged downwash velocity $(\overline{V_v})$ (Figure 21). We observed a substantial increase in $\overline{V_v}$ with increased θ_r . An increase in downwash velocity lowers the effective angle of attack⁴⁰, which could explain the observed reduction in peak C_L with increasing θ_r . However, downwash alone cannot be considered as a sole reason for this change. Further analysis such as pressure distribution between the wings would be needed to understand this discrepancy. In addition, increasing θ_r 518 shifted the formation of peak net circulation to occur early in time, similar to what we observed for peak C_L with increasing θ_r (Figure 4(d)). This was likely on account of the longer time scale ₅₂₀ for θ_r =67.5° (compared to 22.5°), enabling the LEV and TEV to develop in time. These results 521 suggest that rotational motion continuously change the circulation around the wing by diffusing ₅₂₂ the LEV and TEV to remain attached in time. Increasing δ above 10% resulted in lower variation $_{523}$ of $C_{\rm L}$ as well as net circulation around the wing. We see wing-wing interaction effects to diminish for $\delta > 50\%$, thereby behaving like a single wing, which is in agreement with previous studies 16,17 . Increasing the translation angle (θ_t) from 22.5° to 67.5° for δ =10% decreased the net circu-525

₅₂₆ lation by 37% (**Figure 20(c),(d)**). For the same increase in θ_t , we observed $\sim 25\%$ drop in peak

⁵²⁷ lift coefficient (**Figure 9(b),(d)**). In addition, spatially-averaged downwash velocity did not show

₅₂₈ much variation between θ_t =22.5° and 67.5° (**Figure 21(c),(d)**). With changing δ for θ_t =22.5°,

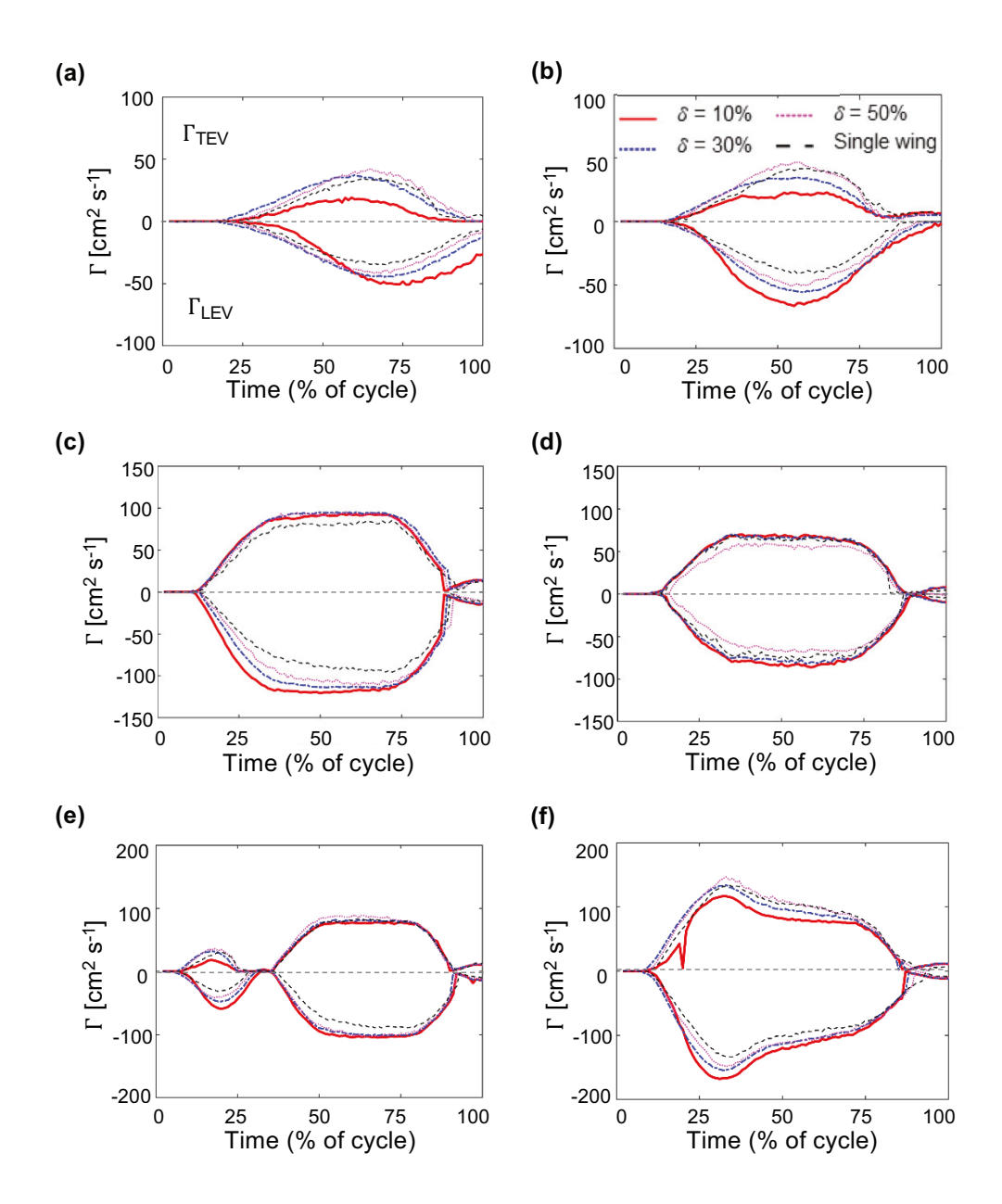


FIG. 20. Circulation (Γ) of the leading edge vortex (LEV) and the trailing edge vortex (TEV) as a function of δ and wing kinematics. (a) and (b) show Γ during rotation at θ_r =22.5° and θ_r =67.5°, respectively. (c) and (d) show Γ during linear translation at θ_t =22.5° and θ_t =67.5°, respectively. (e) and (f) show Γ during combined rotation and linear translation at ζ = 25% and ζ =100%, respectively. Positive Γ corresponds to TEV and negative Γ corresponds to LEV. Both single bristled wing and bristled wing pairs are included. For bristled wing pairs, Γ was only calculated on the left-wing. See subsection II G for more details on definition and calculation of Γ . The *y*-axis range for (a) and (b) is -100 to 100, (c) and (d) is -150 to 150, (e) and (f) is -200 to 200.

₅₂₉ early stages of translation showed noticeable variation in $C_{\rm L}$. However, during constant velocity translation, we observed little to no variation in C_L for $\delta > 30\%$. A similar trend was observed for ₅₃₁ net circulation during linear translation with increasing δ , where $\Gamma_{LEV} > \Gamma_{TEV}$ in time and circu-₅₃₂ lation was essentially unchanged during most of constant velocity translation across all δ (Figure 20B(c),(d)). This implies that initial wing motion helps in development of the LEV and TEV around the wing, and increasing δ decreases the strength of both the LEV and TEV. The results further imply that constant velocity translation resulted in constant rate of change of fluid velocity at both LEV and TEV, which resulted in constant circulation of LEV and TEV (Figure 20(c),(d)). Increasing the overlap (ζ) from $\zeta=25\%$ to 100% for $\delta=10\%$ increased both Γ_{LEV} and Γ_{TEV} , with peak net circulation being increased by $\sim 15\%$ (Figure 20(e),(f)). Peak C_L also increased by 49% with increasing $\zeta=25\%$ to 100% (**Figure 14(b),(d)**), while $\overline{C_L}$ increased by 20% (**Fig**ure 14(f)). This substantial increase in lift coefficients is attributed to the generation of stronger LEVs for ζ =100%. This suggests that rotational acceleration during overlapping motion helps in 542 early development of vortices. Additional acceleration from translation allowed vorticity to diffuse ₅₄₃ at both LE and TE rather than increasing its magnitude. For ζ =100%, right after 25% of cycle 544 time, we see a drop in $C_{\rm L}$ that can be attributed to increased downwash velocity at the same instant 545 (Figure 21(f)).

546 B. Implications of pressure distribution on drag force generation

Examining the pressure distribution on a single wing in rotation (**Figure 7**), we can observe that the formation of a LEV creates a low pressure region on the upper surface of the wing and a positive pressure region on the lower surface. This pressure distribution over a single rotating wing was in agreement with those reported by Cheng and Sun². For a bristled wing pair in rotation with varying δ (**Figure 8**), we see a negative pressure region at the top closer to the LEs and positive pressure distribution at the bottom near the TEs. In the cavity between the wings, pressure was zero to start with and becomes positive instead of negative for all δ during rotation. These results are in contrast with those of Cheng and Sun², where a negative pressure distribution was observed in between the wings at the start of fling. We suspect the positive pressure distribution in the cavity was due to strong viscous forces acting between the plates, which in turn tremendously increase drag.

With increasing time, the positive pressure region diminished with increasing distance between

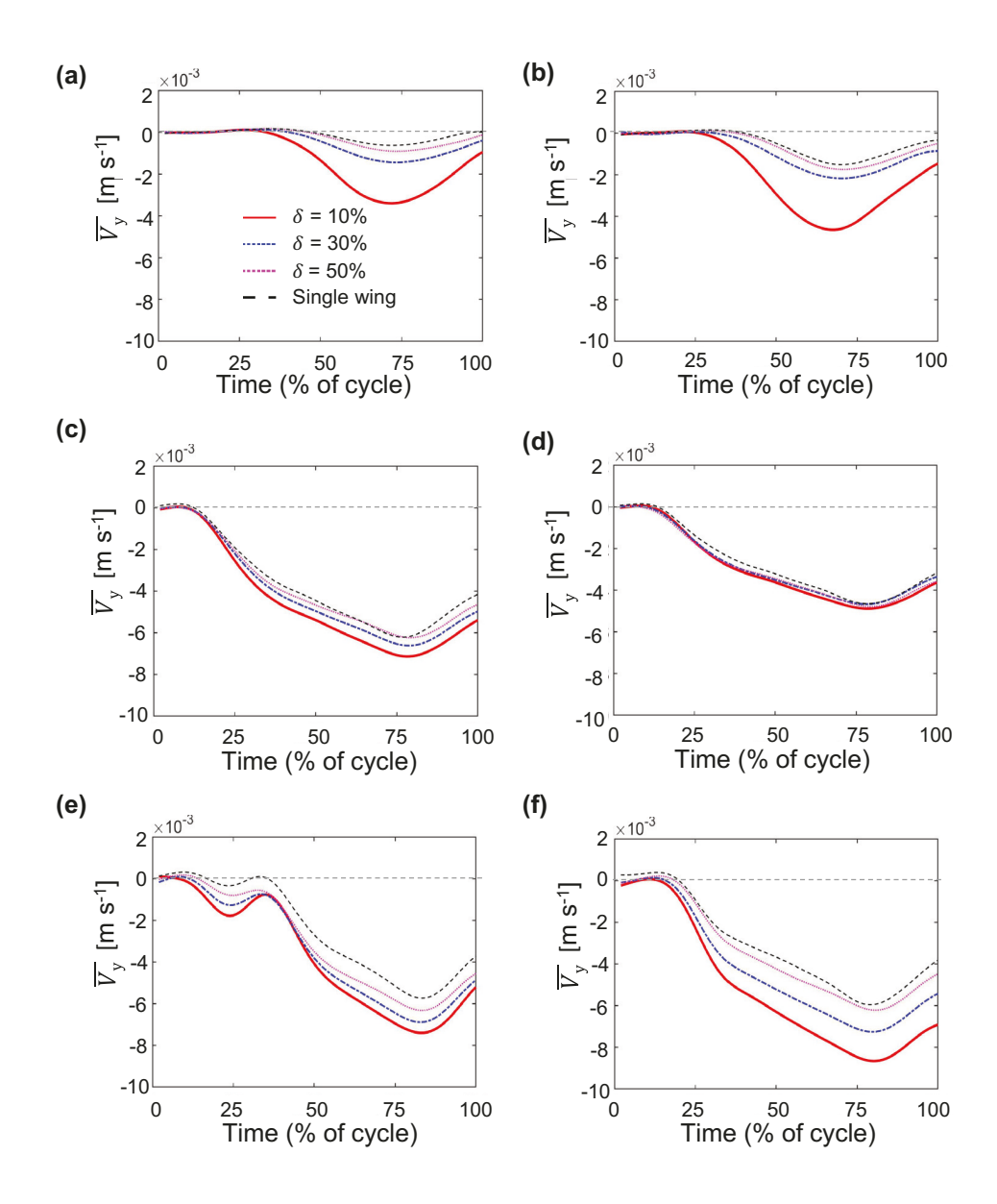


FIG. 21. Time-variation of downwash $(\overline{V_y})$, defined as the spatially-averaged velocity of the flow displaced vertically downward due to wing motion, as a function of δ and wing kinematics. (a) and (b) show $\overline{V_y}$ during rotation at θ_r =22.5° and θ_r =67.5°, respectively. (c) and (d) show $\overline{V_y}$ during linear translation at θ_t =22.5° and θ_t =67.5°, respectively. (e) and (f) show $\overline{V_y}$ during combined rotation and linear translation at ζ =25% and ζ =100%, respectively. Both single bristled wing and bristled wing pairs are included. See subsection II G for more details on definition and calculation of downwash.

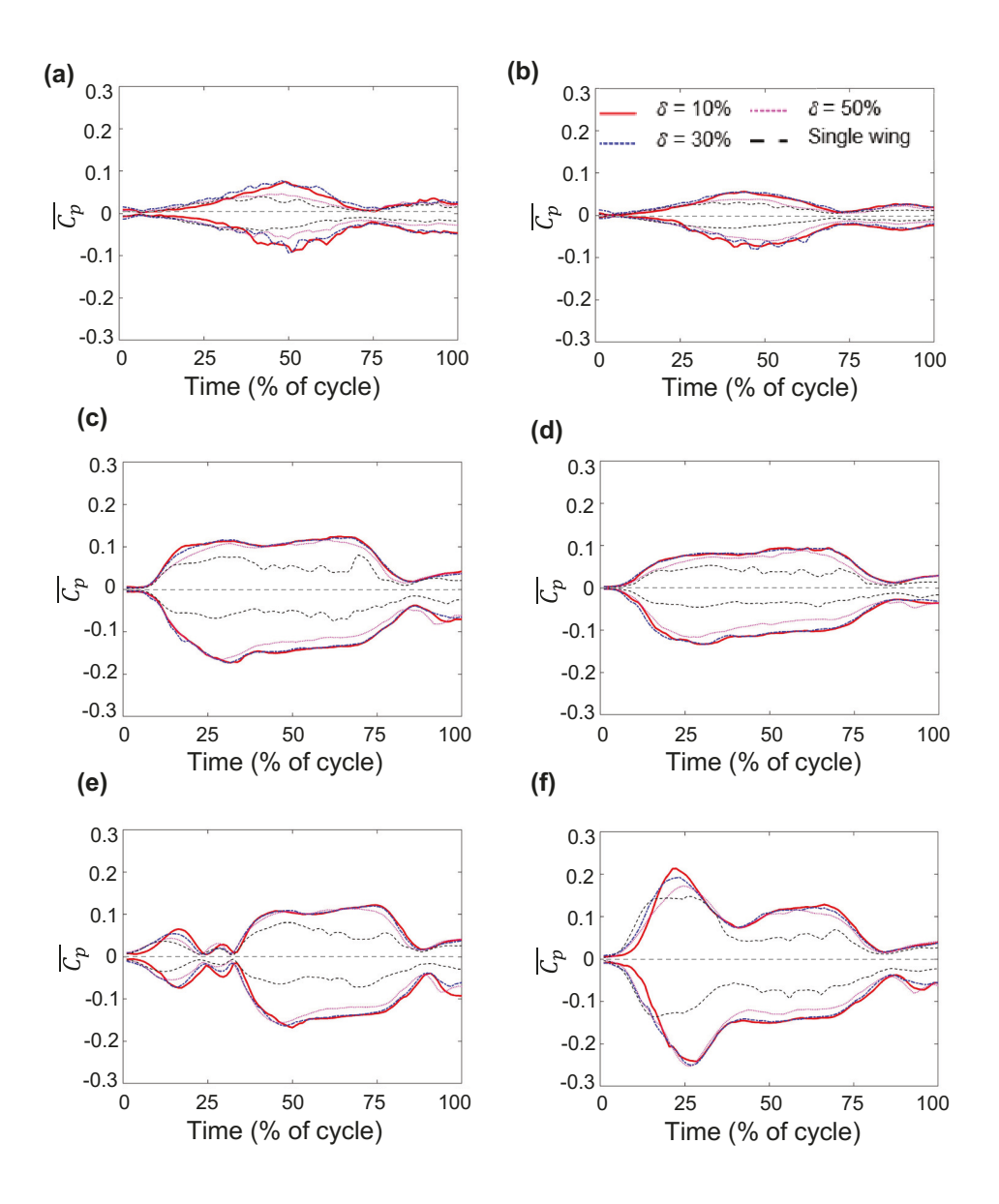


FIG. 22. Time-variation of spatially-averaged pressure coefficient ($\overline{C_p}$) characterizing the total dimensionless pressure distribution in the flow field, as a function of δ and wing kinematics. (a) and (b) show $\overline{C_p}$ during rotation at θ_r =22.5° and θ_r =67.5°, respectively. (c) and (d) show $\overline{C_p}$ during linear translation at θ_t =22.5° and θ_t =67.5°, respectively. (e) and (f) show $\overline{C_p}$ during combined rotation and linear translation at ζ =25% and ζ =100%, respectively. Both single bristled wing and bristled wing pairs are included. See subsection II G for more details on definition and calculation of $\overline{C_p}$.

the wings. The inter-wing distance in time decreases with increasing δ . This suggests that smaller δ plays a crucial role in establishing the time-varying pressure field between the wings. The observed time-variation of spatially-averaged positive pressure coefficient ($\overline{C_p}$) was likely influenced by the positive pressure region in the cavity (**Figure 22(a)**). Increasing θ_r from 22.5° to 67.5° decreased the magnitude of positive pressure inside the cavity which explains the drop in C_D (**Figure 22(a),(b)**). This drop in C_D could be one of the reason for thrips to flap their wings at large rotational angles or low pitch angles 2 (about 20°, equivalent to $\theta_r \approx 70^\circ$). Note that pitch angle was defined relative to the horizontal in Cheng and Sun², unlike how θ_r was defined (relative to the vertical) in this study.

For smaller θ_t and for all δ that was examined here, we observed positive pressure in the cavity between the wings during early stages of linear translation of a bristled wing pair. With time, this positive pressure distribution slowly diminished as the LEs moved apart by ~ 1.5 chord lengths. A negative pressure distribution was found to develop at the top of the wings. Interestingly, we did not see positive pressure distribution in the cavity for θ_t =67.5° even at smaller δ . We suspect that this could be due to a drop in the viscous forces acting in the cavity. Increasing θ_t was observed to decrease the magnitude of both positive and negative $\overline{C_p}$ (**Figure 22(c),(d)**), which explains the substantial drop in C_D for larger θ_t . From a recent study examining thrips wing kinematics³, it was found that they operate at large θ_t values, i.e., they pitch their wings to very low angles (about 30°, equivalent to θ_t =60°) at the start of translation.

Similar to rotation and linear translation, we observed the formation of positive pressure region in the cavity between the wings during initial stages of wing motion for all ζ and all δ values. This positive pressure was found to diminish once the wings started moving apart. The distance between the wings where positive pressure started to diminish was found to depend on wing velocity and δ . Increasing ζ increased both positive and negative $\overline{C_p}$ (**Figure 22(e),(f)**), which was also observed in the force coefficients.

584 C. Cycle-averaged circulation and pressure characteristics: implications on force generation

We next examine cycle-averaged vorticity and pressure distributions for all test conditions and discuss how these factors impact lift generation.

 $\underline{Varying \ \theta_{r}}$ Cycle-averaged net circulation on a wing $(\overline{\Gamma}_{net})$ was calculated using equation (6) for

interacting bristled wing pairs and a single bristled wing as a function of δ and θ_r (**Figure 23(a)**). Irrespective of θ_r , increasing δ resulted in decreasing $\overline{\Gamma_{\rm net}}$ on a bristled wing. As the net circulation over a wing is related to lift generation, the loss of $\overline{\Gamma_{\rm net}}$ with increasing δ can explain the observed reduction of cycle-averaged lift coefficient ($\overline{C_L}$) with increasing δ (**Figure 4(f)**). This association between loss of $\overline{\Gamma_{\rm net}}$ and $\overline{C_L}$ with increasing δ was not established in previous studies of solid wing

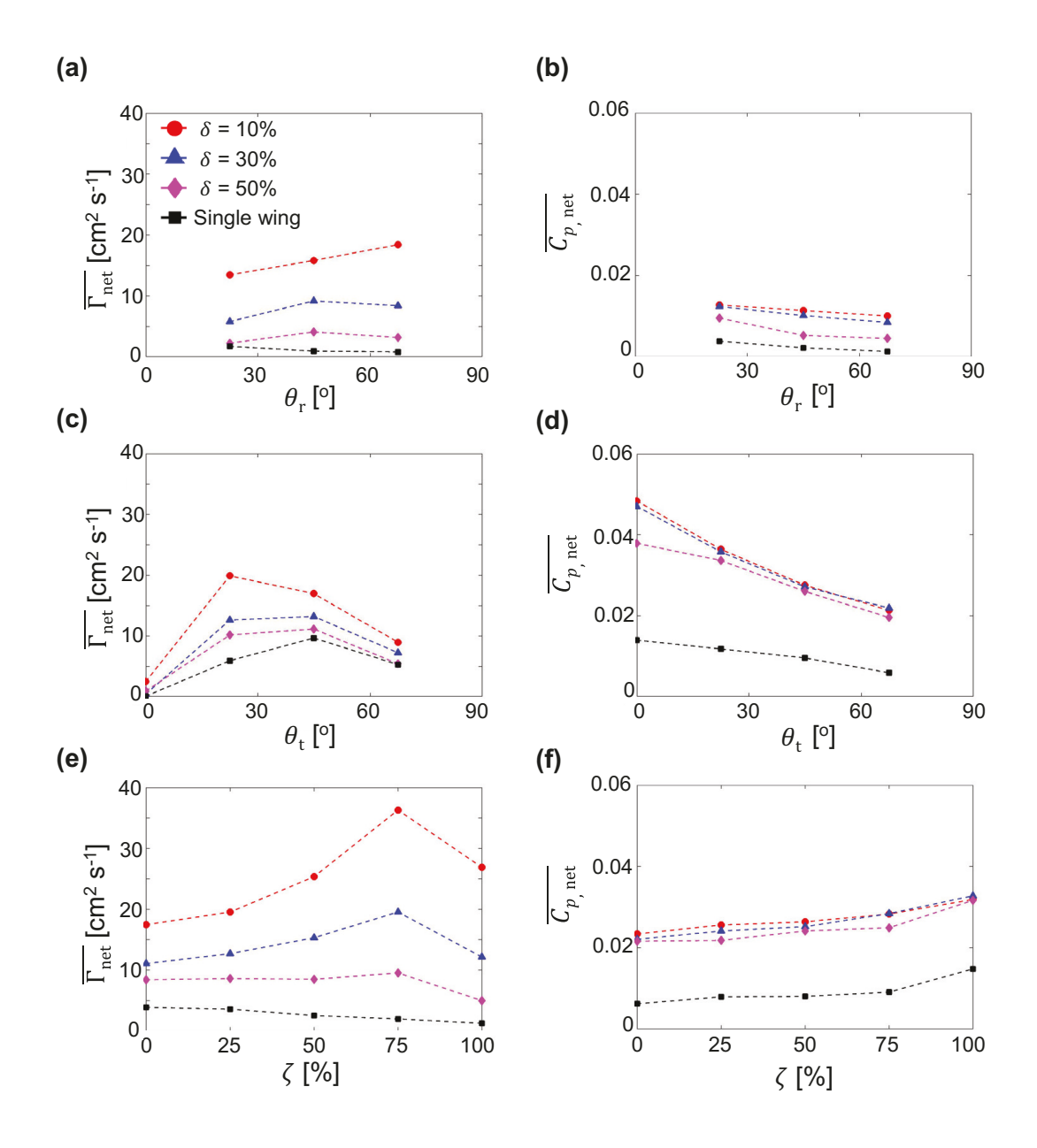


FIG. 23. Cycle-averaged net circulation ($\overline{\Gamma}_{net}$) and cycle-averaged net pressure coefficient, $\overline{C}_{p,net}$ during (a, b) pure rotation (θ_r), (c, d) pure translation (θ_t) and (e, f) overlap (ζ) of bristled wing model at Re=10. Legends for each plot are shown in (a).

pairs 17,41,42 . For a bristled wing pair, dissimilar trends were observed when comparing how $\overline{\Gamma}_{\text{net}}$ and θ_{r} (**Figure 23(a),(b)**) individually affected corresponding \overline{C}_{L} . \overline{C}_{L} decreased with increasing θ_{r} (**Figure 4(f)**), which is in disagreement with how $\overline{\Gamma}_{\text{net}}$ changed with increasing θ_{r} (**Figure 23(a)**). This suggests that circulatory lift alone cannot be used to explain lift generation during rotation of a bristled wing pair at low Re. We need to consider non-circulatory lift mechanisms, including added mass affects, delayed stall at high rotational angles and pressure distribution between the wings during fling.

Cycle-averaged net pressure coefficient ($\overline{C_{p, net}}$) was calculated using equation (11)) for each test condition of θ_r (Figure 23(b)). $\overline{C_{p, net}}$ generally decreased with increasing θ_r , which was analogous to the variation in $\overline{C_D}$ with θ_r . It is important to note that the pressure coefficient on the wings is indicative of total force generated rather than only the drag force. Both wings were in close proximity of each other throughout the entire cycle of rotational motion for any δ tested in this study ($\delta \leq 50\%$), which is conducive for aerodynamic interaction. As a consequence, the pressure distribution of one wing is expected to influence the pressure distribution (and thus lift generation) of both wings of the wing pair (Figure 8). Therefore, despite the lack of decrease in δ_{00} $\overline{\Gamma_{net}}$ with increase in θ_r , we conjecture that decrease in $\overline{C_L}$ with increasing θ_r is due to decrease in $\overline{C_{p,net}}$ with increasing θ_r .

Varying θ_t . Similar to varying θ_r , increasing δ resulted in decreasing $\overline{\Gamma}_{net}$ on a bristled wing (Figure 23(c)) for each θ_t examined in this study. Irrespective of δ , mostly similar trends were observed for both $\overline{\Gamma}_{net}$ (Figure 23(b)) and \overline{C}_L (Figure 9(f)) when varying θ_t . However, peak $\overline{\Gamma}_{net}$ for $\delta = 10\%$ was observed at $\theta_t = 22.5^\circ$, while peak \overline{C}_L for the same δ occurred at about $\theta_t = 45^\circ$. To further explain force generation at $\delta = 10\%$, we examined the pressure distribution.

 $\overline{C_{p,\mathrm{net}}}$ trend for varying θ_t (**Figure 23(d)**) was analogous to the corresponding trend of $\overline{C_D}$ (**Figure 9(e)**). As mentioned in the previous paragraph, variation of $\overline{\Gamma_{\mathrm{net}}}$ with θ_t was similar to fit that of $\overline{C_L}$ for $\delta > 10\%$. Therefore, we focus exclusively on $\overline{C_{p,\mathrm{net}}}$ variation with θ_t for $\delta = 10\%$. From pronounced wing-wing interaction at $\delta = 10\%$ is expected for $\theta_t = 0^\circ$ on account of physical proximity of the wings. Both $\overline{C_L}$ (**Figure 9(f)**) and $\overline{\Gamma_{\mathrm{net}}}$ (**Figure 23(c)**) for this case (i.e., $\delta = 10\%$ and $\theta_t = 0^\circ$) were markedly small. This suggests that circulatory lift can reasonably explain lift generation. The small value of $\overline{C_L}$ for $\theta_t = 0^\circ$ is expected because of the wings being oriented at θ_{c23} 90° angle of attack relative to the horizontal, which promotes LEV-TEV symmetry and has also θ_{c24} been reported in previous studies at similar $Re^{18,20}$. By contrast, both $\overline{C_{p,\mathrm{net}}}$ (**Figure 23(d)**) and $\overline{C_D}$ (**Figure 9(e)**) were large for $\theta_t = 0^\circ$, implying that changes in pressure distribution primarily influ-

626 ences $\overline{C_D}$ for θ_t =0°. $\overline{\Gamma_{net}}$ (**Figure 23(c**)) increased for θ_t =22.5° with corresponding increase in $\overline{C_L}$ (**Figure 9(f)**). Similar to θ_t =0°, circulatory lift is adequate to explain lift generation at θ_t =22.5°. 628 We observed a significant drop in $\overline{C_{p,net}}$ for θ_t =22.5° (**Figure 23(d)**) corresponding to decrease $\overline{C_D}$ (**Figure 9(e)**). Both $\overline{C_{p,net}}$ and $\overline{\Gamma_{net}}$ (**Figure 23(c),(d)**) decreased for θ_t = 45°, unlike the observed increase in $\overline{C_L}$ for θ_t =45° (**Figure 9(f)**). As wing-wing interaction would be weaker for θ_t =45° as compared to θ_t <45° due to larger inter-wing separation in the former case, we expect that the pressure distribution on an individual wing would also assist in its lift generation along with circulatory lift. The observed increase in $\overline{C_L}$ at θ_t =45° (**Figure 9(f)**) can be explained by the containt of $\overline{C_{p,net}}$ at this θ_t relative to circulatory lift generation at θ_t =22.5°. With further increase in θ_t (>45°), both $\overline{C_{p,net}}$ and $\overline{\Gamma_{net}}$ decreased and these resulted in decreasing $\overline{C_L}$ (**Figure 9(f)**). 636 Although $\overline{C_{p,net}}$ and $\overline{\Gamma_{net}}$ would contribute to lift generation for θ_t >45°, we suspect the decrease in $\overline{C_L}$ is due to significant decrease in magnitudes of $\overline{C_{p,net}}$ and $\overline{\Gamma_{net}}$.

Figure 23(e)) for each condition of ζ . $\overline{C_L}$ increased with increasing ζ from 0% to 100% (Figure 14(f)), but $\overline{\Gamma_{net}}$ increased until ζ =75% and then decreased with increasing ζ to 100%. Surprisingly, $\overline{\Gamma_{net}}$ decreased with increasing ζ for a single wing. For smaller ζ , wings initially rotate for a period of time before translating away from each other and permit wing-wing interaction due to the wings being in close proximity. However, for ζ =100%, both wings start to 100% is weakest for ζ =100% and could account for the drop in $\overline{\Gamma_{net}}$ for this ζ . As circulatory lift was not 100% adequately able to explain list generation across the entire range of ζ examined here, we examined 100% the pressure distribution.

 $\overline{C_{p,\mathrm{net}}}$ trend for varying ζ (**Figure 23(f)**) was analogous to the corresponding trend in $\overline{C_{\mathrm{D}}}$ (**Figure 14(e)**). However, we observed a sudden increase in $\overline{C_{p,\mathrm{net}}}$ for ζ =100% across all of the δ values that we tested. This increase in $\overline{C_{p,\mathrm{net}}}$ can explain the increase in $\overline{C_{\mathrm{L}}}$ when ζ is increased from 75% to 100%. Although we observed decrease in $\overline{\Gamma_{\mathrm{net}}}$ with increasing ζ for a single wing, $\overline{C_{p,\mathrm{net}}}$ increased along with $\overline{C_{\mathrm{L}}}$ and $\overline{C_{\mathrm{D}}}$. Collectively, these results show the importance of considering pressure distribution over the wings to understanding force generation by a bristled wing pair in fling.

655 D. Limitations

Although we examined aerodynamic performance of bristled wings in fling for varying kine-656 matics, our study is limited to 2D motion. This simplification was justified by considering the phase of flapping motion where wing-wing interaction at smaller δ is observed. An important question that remains to be investigated is whether the trends that we observed using 2D kinematics are retained when examining 3D flapping kinematics at low Re. A previous study by Santhanakrishnan et al.²⁰ reported that in the *Re* range relevant to the flight of the smallest insects $(Re \le 32)$, spanwise flow decreased and viscous diffusion increased for a revolving non-bristled elliptical wing (3D motion). It is unknown how their observations would be affected by the inclusion of wing bristles and when considering realistic (3D) flapping kinematics of tiny insects. Specifically, large deviations from the stroke plane have been reported in free-flight recordings of 666 thrips³ and shown to be important for vertical force generation in tiny insect flight³⁵. The robotic platform used in this study did not permit evaluating changes in deviation. The above questions will be the subject of our future studies. From the biological standpoint, high-magnification freeflight recordings of tiny insects are needed to identify: (a) the range of δ across different species 670 of tiny flying insects, and (b) whether tiny insects can modulate δ between cycles of flapping flight 671 to tailor their aerodynamic performance.

672 E. Conclusions

Aerodynamic forces and flow structures generated by a single bristled wing and a bristled wing force pair undergoing rotation about the TE(s), linear translation at a fixed angle and their combination were investigated for varying initial inter-wing spacing at Re=10. Irrespective of θ_r , θ_t and ζ , for increasing δ in a bristled wing pair decreased drag by a larger extent as compared to lift reduction due to weakening wing-wing interaction, resulting in the wing pair behaving as two single wings. During wing rotation (θ_r) at smaller δ , positive pressure on the leading surface of each interacting wing (ventral surface) diffused through the inter-bristle gaps due to large viscous forces. This resulted in the formation of a strong +ve pressure region in between the wings, necessitating large drag force to move the wings apart. The positive pressure region diminished with increasing θ_r , which in turn reduced drag forces. This finding suggests that a likely reason for tiny insects to employ large rotational angles (relative to vertical) in fling² is to reduce drag. Finally, we find that

rotational acceleration of a bristled wing aids in early development of LEV and TEV. Previous studies 7,22 have reported δ ranges from 10% to 25% in thrips based on free-flight recordings. Lift was largest for δ =10% across all wing kinematics that were tested in this study, which also falls within the above observed range of δ in thrips.

688 SUPPLEMENTARY MATERIAL

See the supplementary material for: **Movies 1-3** of velocity vector fields overlaid on *y*-vorticity contours showing lack of *z*-directional flow along the x-z plane; **Movies 4-6** showing velocity vector fields overlaid on 2D divergence contours for validating 2D flow simplification; and **Figure S1** showing the validation of using 15% cutoff in circulation calculation.

693 ACKNOWLEDGMENTS

⁶⁹⁴ This work was supported by the National Science Foundation (CBET 1512071 to A.S.).

695 DATA AVAILABILITY STATEMENT

The data that supports the findings of this study are available within the article and in electronic supplementary material.

698 Appendix A: Details on robotic platform

The experimental setup consists of a scaled-up bristled wing pair (or a single bristled wing) mimmersed in a 510 mm (length)×510 mm (width)×410 mm (height) optically clear acrylic tank filled with glycerin. Each wing was attached to a stainless steel D-shaft (diameter=6.35 mm) using custom made L-brackets²³. Uniaxial strain gauges were mounted on the L-brackets to measure lift and drag forces. Two 2-phase hybrid stepper motors with integrated encoders (ST234E, National Instruments Corporation, Austin, TX, USA) were used to drive the D-shaft to perform rotational and translational motion. Rotational motion was achieved using a bevel gear coupled to a motor and a D-shaft, while translational motion was achieved using a rack-and-pinion mechanism driven by a second motor. All the stepper motors (4 motors needed for a bristled wing pair, 2 motors

needed for a single wing) were controlled using a multi-axis controller (PCI-7350, National Instruments Corporation, Austin, TX, USA) via a custom LabVIEW program (National Instruments Corporation, Austin, TX, USA).

711 Appendix B: Modeling of wing kinematics

As mentioned in subsection II C, we used the kinematics developed by Miller and Peskin¹⁸ in this study. We used a sinusoidal velocity profile for wing rotation. The peak angular velocity was maintained constant for each angle of wing rotation (θ_r , in radians) and given by the following equation:

$$\omega_{\text{max}} = \frac{2\theta_{\text{r}} U_{\text{max}}}{\Delta \tau_{\text{rot}} c} \tag{B1}$$

where $\Delta \tau_{\rm rot}$ represents the dimensionless duration of rotational phase, c is the wing chord length and $U_{\rm max}$ (=0.157 m s⁻¹) is the maximum velocity during wing rotation and linear translation. We maintained the ratio of $\theta_{\rm r}$ to $\Delta \tau_{\rm rot}$ constant at 0.4514 to obtain a constant $\omega_{\rm max}$. The cycle time (T) for each $\theta_{\rm r}$ was calculated using the following equation (T values provided in Table I):

$$T = \frac{\Delta \tau_{\text{rot}} c}{U_{\text{max}}} \tag{B2}$$

For example, when $\theta_r = 45^\circ = \pi/4$ rad, we obtain $\Delta \tau_{rot} = (\pi/4*0.4514)=1.74$. The corresponding cycle time, $T_{\theta_r=45^\circ}=1.74\times0.045\times1000)/0.157$ m s⁻¹=498 ms. Rounding off to nearest multiple of 10, we obtain 500 ms.

For wing translation at a fixed angle (θ_t , in radians), we employed a trapezoidal velocity profile consisting of an acceleration phase, constant velocity phase and a deceleration phase. The dimensionless duration ($\Delta \tau$) of each of these phases were maintained constant at 1.3. The cycle time (T) for each translation phase was calculated from equation B2, using $\Delta \tau$ in place of $\Delta \tau_{rot}$: $T=1.3\times0.045\times1000/0.157=373$. Rounding off to nearest multiple of 10, we obtain 370 ms. Total cycle time (T) in translation, for each θ_t , is given by $3\times370=1110$ ms (T values provided in Table I).

The cycle time (*T*) for varying levels of overlap (ζ , ranging between 0% and 100%) between r₃₁ rotation (at θ_r =45°) and start of translation (θ_t =45°) was calculated using the following equation:

$$T_{\zeta} = \left(\frac{100 - \zeta}{100}\right) T_{\theta_{\rm r} = 45^{\circ}} + T_{\theta_{\rm t} = 45^{\circ}}$$
 (B3)

where T_{ζ} represents cycle time for a specific ζ , $T_{\theta_{\rm r}=45^{\circ}}$ and $T_{\theta_{\rm t}=45^{\circ}}$ represents cycle time of wing undergoing rotation to $\theta_{\rm r}$ and translation at $\theta_{\rm t}=45^{\circ}$. For example, when $\zeta=25\%$, we obtain $T_{\zeta}=100$

 $_{734}$ (100-25)/100×500+1110 ms=1485 ms. Rounding off to nearest multiple of 10, we obtain 1490 ms. Similarly, T was calculated for other ζ values (provided in Table I).

736 Appendix C: Details of force measurements

Two different, custom L-brackets were used for non-simultaneous acquisition of normal and 737 tangential forces (**Figure 3(b)**) that were subsequently used for calculating lift and drag forces. The design of lift and drag L-brackets and validation of the methodology can be found in Kasoju et al.²³. Normal and tangential forces (and thus lift and drag forces) were only measured on one 741 wing in tests involving a bristled wing pair, with the assumption that the forces generated by the 742 other wing would be equal in magnitude (as the motion was symmetric for both wings of a wing 743 pair). A pause time of 30 seconds was included between one cycle to the next cycle, in order to 744 exclude any mechanical disturbance between cycles (e.g., sudden bending of L-bracket when the wings come to rest quickly). The raw voltage data was acquired using a data acquisition board (NI USB-6210, National Instruments Corporation, Austin, TX, USA) once the LabVIEW program (used for driving the motors) triggered to start the recording. Force data and angular position of the wings were acquired during each cycle at a sample rate of 10 kHz for all the test conditions mentioned in subsection IID. The raw data was processed in the same manner as in our previous studies^{23,24} and implemented via a custom MATLAB script. A third order low-pass Butterworth filter with a cutoff frequency of 24 Hz was first applied to the raw voltage data. The baseline offset (obtained with wing at rest) was averaged in time and subtracted from the filtered voltage data. The lift and drag brackets were calibrated manually, and the calibration was applied to the filtered voltage data obtained from the previous step to calculate tangential (F_T) and normal (F_N) forces (Figure 3(b)). Lift and drag forces were calculated as components of F_T and F_N as described in 756 subsection II G.

757 Appendix D: 2D TR-PIV

⁷⁵⁸ 2D TR-PIV measurements were performed to visualize the flow structures generated by bristled visualize in rotation, linear translation and their combination for varying δ . The glycerine solution was seeded with 55 μ m diameter titanium dioxide filled polyamide particles (density=1.2 g cm⁻³, LaVision GmbH, Göttingen, Germany). Seeding particles were mixed in the glycerin solution at

162 least one day before TR-PIV data acquisition to allow adequate time to realize homogenous initial distribution. The flow field was illuminated using a 527 nm wavelength single cavity Nd:YLF high-speed laser with a maximum repetition rate of 10 kHz and pulse energy of 30 mJ (Photonics Industries International, Ronkonkoma, NY, USA). This laser provided a 0.5 mm diameter beam that was passed through a -20 mm focal length plano-concave cylindrical lens to generate a 3 mm thick laser sheet, which was then oriented horizontally along the mid-span (HP in **Figure 2A**). Raw TR-PIV images for each of the test conditions were acquired using a high-speed complementary metal-oxide-semiconductor (CMOS) camera (Phantom Miro 110, Vision Research Inc., Wayne, NJ, USA) with a spatial resolution of 1280×800 pixels, maximum frame rate of 1630 frames s⁻¹, and pixel size of 20×20 microns. A 50 mm constant focal length lens (Nikon Micro Nikkor, Nikon Corporation, Tokyo, Japan) was attached to the TR-PIV camera with the aperture set to 1.4 for all the measurements. A digital pulse was generated with a LabVIEW program to use as a trigger to begin recording TR-PIV images synchronized to the start of wing motion. For each of the steet conditions, 100 images were acquired per cycle for 5 consecutive cycles using frame rates specified in Table I.

777 Appendix E: 2D PL-PIV

The wing span at a plane located at $0.5L_b$ measured from the LE (VP in **Figure 2(b)**). The rearead son for conducting 2D PL-PIV measurements for calculating RFC, as opposed to TR-PIV, was
read to avoid PIV particle distortion due to astigmatism when viewing through a non-planar surface read tank in **Figure 2(a)**) to avoid particle distortion. For a fixed laser plane (VP, x-z plane) and camera
read position (**Figure 2(b)**), the bristles will not always be perpendicular to the laser plane during wing
read as to always have the wing bristles to be perpendicular to laser plane (VP in **Figure 2(b)**). This
read allowed us to visualize inter-bristle flow along a plane perpendicular to the bristles. The same
read seeding particles as those used in TR-PIV were used for PL-PIV measurements. Illumination for
read plane pulse mode where two short laser pulses were emitted at a specified pulse separation inread through the wing the same optics as in TR-PIV.

rated by dt (frame-straddling mode, 1 image/pulse) were acquired for each of the test conditions rated by dt (frame-straddling mode, 1 image/pulse) were acquired for each of the test conditions rated by dt (frame-straddling mode, 1 image/pulse) were acquired for each of the test conditions rated using a scientific CMOS (sCMOS) camera (LaVision GmbH, Göttingen, Germany) with a spatial rate resolution of 2560×2160 pixels and a pixel size of $6.5 \times 6.5 \mu m$. A 60 mm constant focal length lens (same as the lens used in TR-PIV) was attached to the sCMOS camera with the aperture set rate of 2.8 for all PL-PIV measurements. The seeding particles illuminated by the laser sheet were focused using this lens. Similar to TR-PIV, a digital trigger signal was generated for PL-PIV using a custom LabVIEW program. This trigger signal was used as a reference to offset PL-PIV image

For wing rotation kinematics, 2D PL-PIV data were acquired at 25%, 37.5%, 50%, 62.5%, 802 87.5% of cycle time (T) in both bristled and solid wing models (wing pairs separated by δ =10%, 803 30%, 50% and single wing) for each $\theta_{\rm r}$ specified previously in subsection II D. For linear transla-804 tion kinematics, 2D PL-PIV data were acquired at 16%, 33%, 50%, 66%, 83% of cycle time (T) in 805 both bristled and solid wing models (wing pairs separated by δ =10%, 30%, 50% and single wing) 806 for each $\theta_{\rm r}$ specified previously in subsection II D. For combined rotation and linear translation 807 kinematics, 2D PL-PIV data were acquired at 8 equally-spaced time points within the overlapping 808 and translational portions of the cycle on both the bristled and solid wing models (wing pair at 809 δ =10% and single wing) for ζ =25% and 100%. 5 consecutive cycles of PL-PIV raw image pairs 810 were acquired at every instant in the cycle.

811 Appendix F: PIV processing

Raw TR-PIV image sequences and PL-PIV image pairs were processed in DaVis 8.3.0 software (LaVision GmbH, Göttingen, Germany). Multi-pass cross-correlation was performed on the raw PIV images with two passes each on an initial window size of 64×64 pixels and a final window size of 32×32 pixels, each with 50% overlap. Post-processing was performed by rejecting velocity vectors with peak ratio Q less than 1.2. The post-processed 2D velocity vector fields were phase-averaged across 5 consecutive cycles at every time instant where TR-PIV and PL-PIV data were acquired. The phase-averaged 2D velocity vector fields were exported as .DAT files containing: (x,y,u,v) from TR-PIV measurements along the x-y plane; and (x,z,u,w) from PL-PIV measurements along the x-z plane. Note that u,v,w are velocity components along x,y,zcoordinates, respectively. The exported TR-PIV velocity vector fields were further processed to

s22 calculate z-component of vorticity (ω_z) and pressure distribution. Similarly, the exported PL-PIV velocity vector fields were used to estimate the reverse flow capacity of the bristled wing. Visual-s24 ization of exported velocity vector fields was performed using Tecplot 360 software (Tecplot, Inc., Bellevue, WA, USA).

826 Appendix G: Validity of 2D flow simplification

 $\Gamma_{\rm LEV}$, $\Gamma_{\rm TEV}$ and $\overline{\Gamma}_{\rm net}$ presented in this study were obtained using 2D, 2-component TR-PIV measurements. To verify whether 2D flow simplification was valid, we calculated the 2D divergence of the TR-PIV based velocity fields along the x-y plane. In a 2D incompressible flow, the extent of three dimensionality of the flow can be characterized by computing 2D divergence of the velocity field, defined as:

$$\nabla \cdot U = \frac{\partial u}{\partial x} + \frac{\partial v}{\partial y} \tag{G1}$$

832 where U represents the velocity vector represented with u along x-axis and v along y-axis. From 833 the velocity vector fields presented in Figures 5, 6, 10, 11, 15, 16, we can see instances in flow 834 field where there are point sources (vectors pointing away from each other) or point sinks (vectors pointing towards each other). The sign of the divergence represents sources or sinks, which in turn can indicate whether fluid motion was into or out of the plane. A region with positive divergence 837 appears in the velocity field as a point source, while a region with negative divergence appears 838 as a point sink. Divergence was calculated for the velocity fields corresponding to wing rotation ₈₃₉ to $\theta_{\rm r}=22.5^{\circ}$, linear translation at $\theta_{\rm t}=22.5^{\circ}$ and combined rotation and translation (ζ =25%) 840 for initial inter wing spacing (δ) of 10% and also for a single wing. These results are provided as supplementary material (Movies 4, 5, 6). Across all the above test conditions, non-zero divergence (small values) was isolated to small regions of the flow field, suggesting that 2D flow simplification was reasonable for our study. Our 2D flow simplification is also in agreement with a recent study²⁰ of a revolving elliptical wing of similar aspect ratio (\sim 2) as this study, where spanwise flow was 845 reduced for Re<10. It is possible that non-zero divergence in fling of bristled wing pairs, resulting 846 in 3D flow, was promoted by the non-uniform pressure distribution in between the wings. The 847 small non-zero divergence regions that were observed across the wing surface was likely due to 848 flow around the tips of the bristle coincident with the TR-PIV plane (along the z-direction).

REFERENCES

- ¹S. P. Sane, "Neurobiology and biomechanics of flight in miniature insects," Curr. Opin. Neuro-
- biol. **41**, 158–166 (2016).
- ⁸⁵² ²X. Cheng and M. Sun, "Aerodynamic forces and flows of the full and partial clap-fling motions
- ⁸⁵³ in insects," PeerJ **3002** (2017).
- ³Y. Z. Lyu, H. J. Zhu, and M. Sun, "Flapping-mode changes and aerodynamic mechanisms in
- miniature insects," Physical Review E **99** (2019).
- ⁴T. Weis-Fogh, "Quick estimates of flight fitness in hovering animals, including novel mecha-
- nisms for lift production," J. Exp. Biol. **59**, 169–230 (1973).
- ⁵T. Weis-Fogh, "Unusual mechanisms for the generation of lift in flying animals," Sci. Am. 233,
- 859 81-87 (1975).
- ⁶C. P. Ellington, "The aerodynamics of insect flight. iii. Kinematics," Phil. Trans. R. Soc. Lond. B
- **305**, 41–78 (1984).
- ⁷A. Santhanakrishnan, A. K. Robinson, S. Jones, A. A. Low, S. Gadi, T. L. Hedrick, and L. A.
- Miller, "Clap and fling mechanism with interacting porous wings in tiny insects," J. Exp. Biol.
- **217**, 3898–3909 (2014).
- ⁸L. A. Miller and C. S. Peskin, "Flexible clap and fling in tiny insect flight," J. Exp. Biol. **212**,
- 866 3076–3090 (2009).
- ⁹T. Maxworthy, "Experiments on the Weis-Fogh mechanism of lift generation by insects in hov-
- ering flight. Part I. Dynamics of the fling," J. Fluid Mech. 93, 47–63 (1979).
- 869 ¹⁰G. R. Spedding and T. Maxworthy, "The generation of circulation and lift in a rigid two-
- dimensional fling," J. Fluid Mech. 165, 247–272 (1986).
- 871 ¹¹F.-O. Lehmann and S. Pick, "The aerodynamic benefit of wing-wing interaction depends on
- stroke trajectory in flapping insect wings," J. Exp. Biol. **210**, 1362–1377 (2007).
- 873 ¹²M. J. Lighthill, "On the Weis-Fogh mechanism of lift generation," J. Fluid Mech. **60**, 1–17
- 874 (1973).
- 875 13D. Kolomenskiy, H. K. Moffatt, M. Farge, and K. Schneider, "The Lighthill-Weis-Fogh clap-
- 876 fling-sweep mechanism revisited," J. Fluid Mech. **676**, 572–606 (2011).
- ₈₇₇ ¹⁴L. A. Miller and C. S. Peskin, "When vortices stick: an aerodynamic transition in tiny insect
- 878 flight," J. Exp. Biol. 207, 3073–3088 (2004).

- ⁸⁷⁹ ¹⁵S. K. Jones, R. Laurenza, T. L. Hedrick, B. E. Griffith, and L. A. Miller, "Lift vs. drag based
 mechanisms for vertical force production in the smallest flying insects," J. Theor. Biol. 384,
 ⁸⁸¹ 105–120 (2015).
- ⁸⁸² ¹⁶M. Sun and X. Yu, "Aerodynamic force generation in hovering flight in a tiny insect," AIAA Journal **44** (2006).
- with the "clap and fling" motion," Phys. Fluids **26**, 071906 (2014).
- smallest insects," J. Exp. Biol. **208**, 195–212 (2005).
- ¹⁹J. M. Birch, W. B. Dickson, and M. H. Dickinson, "Force production and flow structure of the
 leading edge vortex on flapping wings at high and low Reynolds numbers," J. Exp. Biol. 207,
 ^{1063–1072} (2004).
- A. Santhanakrishnan, S. K. Jones, W. B. Dickson, M. Peek, V. T. Kasoju, M. H. Dickinson, and
 L. A. Miller, "Flow structure and force generation on flapping wings at low Reynolds numbers
 relevant to the flight of tiny insects," Fluids 3, 45 (2018).
- ⁸⁹⁴ ²¹Y. Z. Lyu, H. J. Zhu, and M. Sun, "Aerodynamic forces and vortical structures of a flapping
 ⁸⁹⁵ wing at very low reynolds numbers," Physics of Fluids 31, 041901 (2019).
- ⁸⁹⁶ ²²S. K. Jones, Y. J. J. Yun, T. L. Hedrick, B. E. Griffith, and L. A. Miller, "Bristles reduce the force required to 'fling' wings apart in the smallest insects," J. Exp. Biol. **219**, 3759–3772 (2016).
- ⁸⁹⁸ ²³V. T. Kasoju, C. L. Terrill, M. P. Ford, and A. Santhanakrishnan, "Leaky flow through simplified physical models of bristled wings of tiny insects during clap and fling," Fluids **3**, 44 (2018).
- ⁹⁰⁰ ²⁴M. P. Ford, V. T. Kasoju, M. G. Gaddam, and A. Santhanakrishnan, "Aerodynamic effects of
 ⁹⁰¹ varying solid surface area of bristled wings performing clap and fling," Bioinspir. Biomim 14,
 ⁹⁰² 046003 (2019).
- ₉₀₃ ²⁵A. Y. L. Cheer and M. A. R. Koehl, "Paddles and rakes: fluid flow through bristled appendages of small organisms," J. Theor. Biol. **129**, 17–39 (1987).
- ⁹⁰⁵ ²⁶C. Loudon, B. A. Best, and M. A. R. Koehl, "When does motion relative to neighboring surfaces alter the flow through arrays of hairs?" J. Exp. Biol. **193**, 233–254 (1994).
- ⁹⁰⁷ ²⁷S. Sunada, H. Takashima, T. Hattori, K. Yasuda, and K. Kawachi, "Fluid-dynamic characteris-⁹⁰⁸ tics of a bristled wing," J. Exp. Biol. **205**, 2737–2744 (2002).
- ⁹⁰⁹ ²⁸D. Kolomenskiy, S. Farisenkov, T. Engels, N. Lapina, P. Petrov, F.-O. Lehmann, R. Onishi, ⁹¹⁰ H. Liu, and A. Polilov, "Aerodynamic performance of a bristled wing of a very small insect,"

- 911 Experiments in Fluids **61**, 1–13 (2020).
- 912 ²⁹D. Weihs and E. Barta, "Comb wings for flapping flight at extremely low Reynolds numbers,"
- 913 AIAA J. **46**, 285–288 (2008).
- ₉₁₄ ³⁰G. Davidi and D. Weihs, "Flow around a comb wing in low-Reynolds-number flow," AIAA J.
- **50**, 249–253 (2012).
- 916 31S. H. Lee and D. Kim, "Aerodynamics of a translating comb-like plate inspired by a fairyfly
- 917 wing," Phys. Fluids 29, 081902 (2017).
- 918 ³²S. H. Lee, M. Lahooti, and D. Kim, "Aerodynamic characteristics of unsteady gap flow in a
- bristled wing," Phys. Fluids **30**, 071901 (2018).
- 920 ³³S. H. Lee, M. Lee, and D. Kim, "Optimal configuration of a two-dimensional bristled wing,"
- ⁹²¹ J. Fluid Mech. **888**, A23 (2020).
- ⁹²² ³⁴X. Cheng and M. Sun, "Aerodynamic forces and flows of the full and partial clap-fling motions
- ⁹²³ in insects," PeerJ **5**, e3002 (2017).
- ₉₂₄ ³⁵X. Cheng and M. Sun, "Very small insects use novel wing flapping and drag principle to generate
- the weight-supporting vertical force," Journal of Fluid Mechanics **855**, 646–670 (2018).
- 926 36V. T. Kasoju, M. P. Ford, T. T. Ngo, and A. Santhanakrishnan, "Inter-species
- 927 variation in number of bristles on forewings of tiny insects does not impact clap-
- 928 and-fling aerodynamics," bioRxiv Preprint (2020), doi: 10.1101/2020.10.27.356337,
- 929 https://www.biorxiv.org/content/early/2020/10/27/2020.10.27.356337.full.pdf.
- 930 ³⁷M. Samaee, N. H. Nelsen, M. G. Gaddam, and A. Santhanakrishnan, "Diastolic vortex alter-
- ations with reducing left ventricular volume: an in vitro study," J. Biomech. Eng. 142, 121006
- 932 (2020).
- 933 ³⁸J. O. Dabiri, S. Bose, B. J. Gemmell, S. P. Colin, and J. H. Costello, "An algorithm to estimate
- unsteady and quasi-steady pressure fields from velocity field measurements," J. Exp. Biol. 217,
- 935 331–336 (2014).
- 936 ³⁹S. Mao and Y. Xin, "Flows around two airfoils performing fling and subsequent translation and
- translation and subsequent clap," Acta Mechanica Sinica 19, 103–117 (2003).
- 938 ⁴⁰S. P. Sane, "The aerodynamics of insect flight," J. Exp. Biol. **206**, 4191–4208 (2003).
- 939 ⁴¹M. Sun and X. Yu, "Aerodynamic force generation in hovering flight in a tiny insect," AIAA J.
- 940 **44**, 1532–1540 (2006).
- 941 ⁴²D. Kolomenskiy, H. K. Moffatt, M. Farge, and K. Schneider, "Vorticity generation during the
- olap-fling-sweep of some hovering insects," Theoretical and Computational Fluid Dynamics

24, 209–215 (2010).

944 ⁴³B. L. Smith and D. R. Neal, "Particle image velocimetry," (Crc Press, 2016) pp. 1–27.